

# Tempo2, a new pulsar timing package. II: The timing model and precision estimates

R. T. Edwards\*, G. B. Hobbs, R. N. Manchester

*Australia Telescope National Facility, CSIRO, P.O. Box 76, Epping NSW 1710 Australia*

26 November 2024

## ABSTRACT

TEMPO2 is a new software package for the analysis of pulsar pulse times of arrival. In this paper we describe in detail the timing model used by TEMPO2, and discuss limitations on the attainable precision. In addition to the intrinsic slow-down behaviour of the pulsar, TEMPO2 accounts for the effects of a binary orbital motion, the secular motion of the pulsar or binary system, interstellar, Solar system and ionospheric dispersion, observatory motion (including Earth rotation, precession, nutation, polar motion and orbital motion), tropospheric propagation delay, and gravitational time dilation due to binary companions and Solar system bodies. We believe the timing model is accurate in its description of predictable systematic timing effects to better than one nanosecond, except in the case of relativistic binary systems where further theoretical development is needed. The largest remaining sources of potential error are measurement error, interstellar scattering, Solar system ephemeris errors, atomic clock instability and gravitational waves.

**Key words:** astrometry – celestial mechanics – methods:data analysis – pulsars:general – time

## 1 INTRODUCTION

The core of any pulsar timing software package is the mathematical model for the times of arrival (TOAs) of pulses at the observatory. As the pulsar population grows more diverse and observing systems increase in sensitivity, the accuracy demanded of timing models grows accordingly. For many years the standard choice for pulsar timing was the TEMPO<sup>1</sup> software package. Accurate at the 100-ns level, the timing model of TEMPO was adequate for numerous important discoveries (e.g. Taylor et al. 1979; Taylor & Weisberg 1989; Wolszczan & Frail 1992; Kaspi et al. 1994; van Straten et al. 2001). However, motivated primarily by the possibility of directly detecting gravitational radiation through its effect on pulse arrival times, current observing campaigns are setting highly ambitious goals in terms of data precision and volume. These projects aim to obtain of the order of  $\sim 10^4$  independent TOA measurements with a typical root-mean-square (RMS) uncertainty of 100 ns (e.g. Jenet et al. 2005), dictating a maximum allowable systematic error of 1 ns.

Motivated by the need for improved accuracy as well as greater flexibility in fitting and analysis procedures, we have developed a new pulsar timing package called TEMPO2. The architecture, capabilities and usage of TEMPO2 are described by Hobbs et al. (2006) (hereafter Paper I). The purpose of the present work is to describe the timing model in detail, and provide estimates of the accuracy of each component of the model. Section 2 begins with an overview of the model and definitions of the various relativistic coordinate frames and proper times (Section 2.2). This is followed by an expansion of the complete geometric propagation delay accurate to better than 1 ns (Section 2.3). The remainder of Section 2 discusses all other delay terms in the timing formula, and provides a detailed description of how each contribution is evaluated according to the parameters of the model and other information. Section 3 gives a detailed account of the accuracy with which each term is computed, and discusses possible avenues for further improvement of the timing model. Finally, for the convenience of comparison with the commonly used TEMPO software package, Section 4 details the differences between TEMPO and TEMPO2. Tabular summaries of timing model parameters and variables are provided in the Appendix.

\* Email: Russell.Edwards@csiro.au

<sup>1</sup> <http://www.atnf.csiro.au/research/pulsar/tempo/>

## 2 TIMING MODEL

### 2.1 Overview

Pulsar timing consists of the measurement of the pulse times of arrival (TOAs) at the observatory and the fitting of these TOAs to a model. The timing model relates the measured TOA to the time of emission at the pulsar, from which a “pulse phase of emission” is computed via a model of the intrinsic variations in the pulse period. If the timing model is correct, in the absence of measurement noise all calculated pulse phases will be integer (when expressed in units of cycles or turns). In practise, the parameters of the model are not known a priori, and measurement noise is present, so that the deviations of these pulse phases from the nearest integer (the “residuals”) are finite. Once the timing model parameters are refined to optimise some statistic of the residuals – in TEMPO2 this is the root-mean-square or  $\chi^2$  (see Paper I) – and assuming there are no shortcomings in the structure of the timing model, the residual deviations are due only to measurement noise.

The focus of this paper is the timing model, which relates a measured TOA to a time of emission, and from there computes a corresponding pulse phase of emission. The latter step is described in Section 2.8. The former part comprises the bulk of the complexity of the model, and it too can be helpfully broken into two main parts. Firstly, because that part of the model relates a proper time of arrival at the observatory to a proper time of emission at the pulsar, a general relativistic frame transformation is necessary. This is performed in a sequence of manageable steps, outlined in Section 2.2. Secondly, the light travel time must be accounted for. This is derived in Section 2.3 under the assumption of Euclidean space-time and zero refraction or dispersion. The remaining parts of Section 2 derive in full mathematical detail the various parts of the frame transformation and light travel time, including dispersion, refraction and general relativistic effects along the propagation path.

### 2.2 Coordinate frames and time variables

The relativistic frame transformation between observatory proper time and pulsar proper time is computed in several steps. This section outlines the steps, gives the names of the various reference frames and introduces the notation use to refer to time variables in each frame. The time variable for each frame may appear subscripted with the letter “a” or “e”, where “a” denotes a time of arrival and “e” a time of emission, at the origin of the frame denoted by the superscript. A time variable may also appear without a subscript, meaning that it is an arbitrary coordinate time variable. As such, time variables without subscripts are related by coordinate transformations, whereas subscripted time variables additionally include propagation delays. Spatial 3-vectors are defined in terms of a right-handed Cartesian system.

The pulsar timing procedure begins with a measured arrival time, which after correcting for imperfections in the observatory clock yields a time of arrival  $t_a^{\text{obs}}$ . The clock correction process in TEMPO2 operates through interpolation of tables of measured offsets between pairs of clocks and their variation with time (see Paper I), and includes offsets relating to the fact that observatory clocks usually approximate Coordinated Universal Time (UTC<sup>2</sup>) rather than Terrestrial Time (TT). The corrected arrival time is measured in the TT time scale, which is defined to differ from coordinate time at the geocentre by a constant rate. It should be noted then that times referred to TT are only approximately proper times of the observatory. This transformation to Geocentric Coordinate Time scale (TCG) is done in the same step as transformation to Barycentric Coordinate Time (TCB), so no variable is assigned to this time scale. The spatial part of the terrestrial frame is the International Terrestrial Reference System (ITRS), while the geocentric counterpart is the Geocentric Celestial Reference System (GCRS).

Coordinate times  $t^{\text{SSB}}$  in the frame of the Solar system barycentre (SSB) are obtained by application of the gravitational redshift and special relativistic time dilation integral (“Einstein delay”) described in Section 2.5.1. Coordinate time (TCB) in this frame represents the proper time that would be measured by an observer located at the Solar system barycentre were the gravitational field of the sun and planets not present. The spatial part of the barycentric frame is the Barycentric Celestial Reference System (BCRS), while directions in this frame define the International Celestial Reference System (ICRS). The origin of the BCRS is the SSB, hence  $t_a^{\text{SSB}}$  refers to the arrival time of the pulse at the barycentre.

For further information on the definitions of TT, TCG, TCB, the ITRS, GCRS, BCRS and ICRS, see the Resolutions of the XXIIIrd and XXIVth General Assembly of the International Astronomical Union (IAU; Anderson 1999; Rickman 2001) and the 2003 Conventions of the International Earth Rotation and Reference Systems Service (IERS; McCarthy & Petit 2004).

Tracing the propagation backward toward the source, the next reference frame is that which is co-moving with the pulsar, or if it is a member of a binary system, the binary barycentre (BB). Coordinates in this frame are defined such that the coordinate time  $t^{\text{BB}}$  would be equal to the proper time of an observer at the origin of the frame, were the gravitational field of the pulsar and its companion not present. The transformation of the arrival time to this frame is discussed in Section

<sup>2</sup> Due to copyediting errors, in Paper I the acronyms UTC, TCG, TCB, and TDB were inadvertently referred to as UCT, CGT, BCT and BDT.

2.6.3. The orientation of this frame is chosen such that the Lorentz transformation relating it to the SSB frame is rotation-free, so that to zeroth order the corresponding basis vectors are parallel. The spatial origin of this frame is the BB. The time origin is chosen such that  $t^{\text{BB}}$  has zero offset from  $t^{\text{SSB}}$  at  $t^{\text{BB}} = t^{\text{SSB}} = t_{\text{pos}}$ , where the latter is an epoch of position set by the user.

The time scale for measurements is the proper time  $t^{\text{psr}}$  measured at the pulsar, or more precisely at its centre, were its gravitational field not present. For isolated pulsars  $t^{\text{psr}} = t^{\text{BB}}$ . For binary pulsars,  $t^{\text{psr}} - t^{\text{BB}}$  is the binary Einstein delay (Section 2.7.4). As with the SSB–BB case, the BB–pulsar transformation is rotation-free. The spatial origin of this frame is the centre of gravitational field of the pulsar, so that  $t_e^{\text{psr}}$  is the equivalent time of emission from the centre of the star. This differs from the actual time of emission by (to first order) the light travel time to the true point of emission, which is assumed to be stable on the time scale of interest.

### 2.3 Geometric propagation delay

Although it is convenient to break the propagation delay into separate contributions and treat them in the order in which they occur along the photon path, some terms in the model depend jointly upon the motion of the observatory and the motion of the pulsar (relative to the SSB). For this reason, in this section we derive the complete geometric propagation delay, that is the time of propagation neglecting dispersion, refraction and relativistic delays. The resultant terms are then assigned to different parts of the propagation path and treated in the relevant sections below.

The geometric propagation delay is simply the Euclidean distance from the observatory to the pulsar, divided by the vacuum speed of light,  $c$ . The displacement vector from the observatory to the pulsar is the sum of the barycentric position of the observatory ( $\mathbf{r}$ ), the barycentric position of the pulsar (or BB) ( $\mathbf{R}_0$ ) at a given epoch ( $t_{\text{pos}}$ ), the position of the pulsar with respect to the BB ( $\mathbf{b}$ , zero for isolated pulsars), and the displacement ( $\mathbf{k}$ ) of the binary barycentre (or the pulsar itself, if isolated) in the time elapsed since the epoch  $t_{\text{pos}}$ , owing to the initial velocity of the system (relative to the SSB) and acceleration in the Galactic or cluster gravitational field:

$$\mathbf{R} = \mathbf{R}_0 + \mathbf{b} + \mathbf{k} - \mathbf{r}. \quad (1)$$

Squaring equation (1) and expanding the square root to third order,

$$|\mathbf{R}| = \left[ |\mathbf{R}_0|^2 + |\mathbf{b}|^2 + |\mathbf{k}|^2 + |\mathbf{r}|^2 + 2(\mathbf{R}_0 \cdot \mathbf{b} + \mathbf{R}_0 \cdot \mathbf{k} - \mathbf{R}_0 \cdot \mathbf{r} + \mathbf{b} \cdot \mathbf{k} - \mathbf{b} \cdot \mathbf{r} - \mathbf{k} \cdot \mathbf{r}) \right]^{1/2} \quad (2)$$

$$= |\mathbf{R}_0| + A - \frac{A^2}{2|\mathbf{R}_0|} + \frac{A^3}{2|\mathbf{R}_0|^2} + \dots, \text{ where} \quad (3)$$

$$A = \frac{1}{2|\mathbf{R}_0|} \left[ |\mathbf{b}|^2 + |\mathbf{k}|^2 + |\mathbf{r}|^2 + 2(\mathbf{R}_0 \cdot \mathbf{b} + \mathbf{R}_0 \cdot \mathbf{k} - \mathbf{R}_0 \cdot \mathbf{r} + \mathbf{b} \cdot \mathbf{k} - \mathbf{b} \cdot \mathbf{r} - \mathbf{k} \cdot \mathbf{r}) \right]. \quad (4)$$

Neglecting terms of order  $|\mathbf{R}_0|^{-3}$  and denoting the initially radial and transverse components of each vector using subscripts, i.e.  $a_{\parallel} = \mathbf{a} \cdot \mathbf{R}_0$ ,  $\mathbf{a}_{\perp} = \mathbf{a} - a_{\parallel} \mathbf{R}_0 / |\mathbf{R}_0|$  and hence,  $\mathbf{a}_{\perp} \cdot \mathbf{b}_{\perp} = (\mathbf{a} \times \mathbf{R}_0) \cdot (\mathbf{b} \times \mathbf{R}_0)$ , the following relation is found:

$$|\mathbf{R}| = |\mathbf{R}_0| + k_{\parallel} - r_{\parallel} + b_{\parallel} + \frac{1}{|\mathbf{R}_0|} \left( \frac{|\mathbf{k}_{\perp}|^2}{2} - \mathbf{k}_{\perp} \cdot \mathbf{r}_{\perp} + \mathbf{k}_{\perp} \cdot \mathbf{b}_{\perp} + \frac{|\mathbf{r}_{\perp}|^2}{2} - \mathbf{r}_{\perp} \cdot \mathbf{b}_{\perp} + \frac{|\mathbf{b}_{\perp}|^2}{2} \right) \left( 1 - \frac{k_{\parallel}}{|\mathbf{R}_0|} + \frac{r_{\parallel}}{|\mathbf{R}_0|} - \frac{b_{\parallel}}{|\mathbf{R}_0|} \right) + O(|\mathbf{R}_0|^{-3}). \quad (5)$$

The first four terms in equation (5) are the initial SSB–BB distance (Section 2.6.2), the secular displacement in the initially radial direction (Section 2.6.2), the projection of the observatory–SSB vector on the initial line of sight (Section 2.5.3), and the projection of the binary motion on the initial line of sight (Section 2.7.1). The terms in the first pair of parentheses correspond to the Shklovskii effect (2.6.2), annual proper motion (2.5.3), secular changes in the apparent orbital viewing geometry (2.7.1), annual parallax (2.5.3), annual-orbital parallax (2.7.1) and orbital parallax (2.7.1). The second, third and fourth terms in the second pair of parentheses represent variations in the effects just discussed due to radial motion of the pulsar or binary system, the motion of the Earth around the SSB, and the motion of the pulsar about the BB. Although these terms give rise to an additional eighteen contributions to the timing formula, to reach the stated accuracy goal of 1 ns, for a 20-yr observing campaign on any of the presently known millisecond pulsars only three of them need be considered: the secular change (Section 2.6.2) and annual modulation (Section 2.5.3) of the Shklovskii effect and the secular change of the annual proper motion (Section 2.5.3).

The displacement due to secular motion,  $\mathbf{k}$  may be broken into first and second derivatives:

$$\mathbf{k} = \boldsymbol{\mu} |\mathbf{R}_0| (t^{\text{BB}} - t_{\text{pos}}) + \frac{\mathbf{a}}{2} (t^{\text{BB}} - t_{\text{pos}})^2, \quad (6)$$

where  $\boldsymbol{\mu}$  is the velocity divided by the distance, or in essence a three-dimensional proper motion, and  $\mathbf{a}$  is an acceleration vector accounting for Galactic differential rotation and gravitational acceleration. The acceleration is of order  $\sim 10^{-11} \text{ m s}^{-2}$  (Bell & Bailes 1996), contributing only  $\sim 500 \text{ km}$  to  $\mathbf{k}$  at either end of a 20-year observation campaign centred on  $t_{\text{pos}}$ . Equation (5) can be expanded in terms of this parameterisation of  $\mathbf{k}$ , giving rise to an additional 27 terms. We have estimated

the magnitude of these terms for all pulsars in the ATNF catalogue<sup>3</sup> (Manchester et al. 2005), including an allowance for greater acceleration for pulsars in globular clusters ( $a \sim 10^{-8} \text{ m s}^{-2}$ ; Freire et al. 2001). Only two of the extra terms involving  $\mathbf{a}$  exceed 1 ns for a 20-year observing campaign, the first contributing to  $k_{\parallel}$  and the second contributing to the Shklovskii term of equation (5). For all other terms of equation (5) involving  $\mathbf{k}$  the acceleration is neglected.

## 2.4 Top-level timing formula

Having described the coordinate frames used and derived the basic Euclidean propagation length, it remains to specify the details of the calculation of the various delay terms associated with frame transformations, the vacuum propagation delay, and corrections due to non-unity refractive indices and space-time curvature along the propagation path. For convenience the timing formula is divided into three main contributions, which will be further broken down in the sections that follow:

$$t_e^{\text{psr}} = t_a^{\text{obs}} - \Delta_{\odot} - \Delta_{\text{IS}} - \Delta_{\text{B}}. \quad (7)$$

$\Delta_{\odot}$  (Section 2.5) includes the coordinate transformation to the SSB frame, vacuum propagation delays associated with the Earth’s orbital motion and the spin, precession and nutation of the Earth (on which the observatory is located) and excess delays owing to the passage of the signal through the Earth’s atmosphere and the Solar system. This term relates the measured time of arrival to the TCB arrival time at the SSB:  $t_a^{\text{SSB}} = t_a^{\text{obs}} - \Delta_{\odot}$ .

$\Delta_{\text{IS}}$  (2.6) includes the transformation to the binary barycentre frame, vacuum propagation delays due to the secular motion of the system, and excess propagation delays due to passage of the signal through the interstellar medium. This term relates the TCB time of arrival at the SSB to the BB coordinate time of arrival at the BB:  $t_a^{\text{BB}} = t_a^{\text{SSB}} - \Delta_{\text{IS}}$ .

$\Delta_{\text{B}}$  includes the transformation to the pulsar frame, vacuum delays due to the binary orbital motion, and excess delays due to passage of the signal through the gravitational field of the companion. This term relates the BB coordinate time of arrival at the BB to the pulsar proper time of emission:  $t_e^{\text{psr}} = t_a^{\text{BB}} - \Delta_{\text{B}}$ .

Note that since some of the geometric delay terms involve two of the three components (Solar system, secular or binary) of the relative motion of the observatory and the pulsar, the choice of which of these terms are assigned to each of the three top-level terms is somewhat arbitrary. See Section 2.3 for a detailed listing of where each term is discussed.

Once the time of emission is obtained, it remains to compute the phase of the pulse train at that time. This relationship,  $\phi(t_e^{\text{psr}})$ , is discussed in Section 2.8. For the correct set of model parameters and in the absence of measurement noise, the phase for every computed time of emission is an integer number of cycles (turns). The fractional part of  $\phi(t)$  is the timing residual, which is more often expressed in time units through division by the pulse frequency.

## 2.5 Forming barycentric arrival times

The term denoted  $\Delta_{\odot}$  in equation (7) includes all effects pertinent to the transformation of the observed TOA ( $t_a^{\text{obs}}$ ) to an equivalent time of arrival for the same pulse wave-front at the Solar system barycentre. This in turn can be broken into several steps. These are: atmospheric delays, vacuum retardation due to observatory motion (“Roemer delay” and parallax), excess propagation delay due to dispersion, the effects of relativistic frame transformation (“Einstein delay”), and the excess delay experienced by rays as they pass through the gravitational potential of Solar system bodies (“Shapiro delay”). These terms are denoted as follows:

$$\Delta_{\odot} = \Delta_{\text{A}} + \Delta_{\text{R}\odot} + \Delta_{\text{p}} + \Delta_{\text{D}\odot} + \Delta_{\text{E}\odot} + \Delta_{\text{S}\odot} \quad (8)$$

### 2.5.1 Einstein delay

The space-time coordinates of pulse arrival events are specified in the coordinate frame of the observatory, in which pulse timing anomalies may manifest due to spin and orbital acceleration and variations in gravitational potential. To avoid these effects, pulse arrival events are transformed to the quasi-inertial frame of the Solar system barycentre. The two frames are related by a relativistic four-dimensional space-time transformation. The spatial part of the event is the displacement of the observatory from the geocentre at the instant of reception, which is altered by a negligible amount due to special and general relativistic length contraction. The effects of relativistic time dilation, on the other hand, cannot be neglected. TEMPO2 uses the numerical time dilation results of Irwin & Fukushima (1999), who used the DE405 Solar system ephemeris (Standish 1998) to compute the time dilation integral:

$$\Delta_{\text{E}\odot-\oplus} = \frac{1}{c^2} \int_{t_0}^t \left( U_{\oplus} + \frac{v_{\oplus}^2}{2} + \Delta L_C^{(\text{PN})} + \Delta L_C^{(\text{A})} \right) dt, \quad (9)$$

<sup>3</sup> <http://www.atnf.csiro.au/research/pulsar/psrcat/>

where  $U_{\oplus}$  is the gravitational potential at the geocentre due to all Solar system bodies except the Earth, and  $v_{\oplus}$  is the velocity of the geocentre relative to the Solar system barycentre. The first two terms describe, to order  $1/c^2$ , the gravitational redshift and special relativistic time dilation respectively. These contribute in roughly 2:1 ratio ( $\frac{1}{2}U_{\oplus} \simeq v_{\oplus}^2 \simeq 10^{-8}c^2$ ), for a mean drift of  $\sim 1.5 \times 10^{-8}$ , or  $\sim 0.5$  s yr $^{-1}$ . The main source of time variation in the integrand is due to the orbital acceleration of the Earth, which via conservation of energy causes approximately equal changes (of the same sign) in the first two terms, amounting to  $\sim 3 \times 10^{-10}$  in rate amplitude, or  $\sim 2$  ms in integrated delay amplitude. The remaining terms apply a correction for higher-order relativistic terms ( $\Delta L_C^{(PN)} = 1.097 \times 10^{-16}$ ; Fukushima 1995) and asteroids ( $\Delta L_C^{(A)} = 5 \times 10^{-18}$ ; Fukushima 1995), made in mean rate only.

The time dilation integral of equation (9) relates the coordinate times of clocks at the geocentre and the Solar system barycentre. For observers located on the surface of the Earth, corrections must be made for the differential time dilation and gravitational redshift between the observatory and the geocentre, yielding:

$$\Delta_{E\odot} = \Delta_{E\odot-\oplus} + \frac{\mathbf{s} \cdot \dot{\mathbf{r}}_{\oplus} + W_0 t_a^{\text{obs}}}{c^2}, \quad (10)$$

where  $\mathbf{s}$  is a vector from the geocentre to the observatory,  $\dot{\mathbf{r}}_{\oplus}$  is the velocity of the geocentre with respect to the barycentre, and  $W_0 = 6.969290134 \times 10^{-10}c^2$  approximates the gravitational plus spin potential of the Earth at the geoid. (See Section 2.5.3 for the calculation of  $\mathbf{s}$  and  $\dot{\mathbf{r}}_{\oplus}$ .) Note that, while the value of the potential varies geographically and temporally, the most recent definition of TT (Rickman 2001), the terrestrial time scale to which TEMPO2 refers pulse time of arrival measurements, takes the exact value of  $W_0/c^2$  quoted above as definitive of the rate difference between TT and SI coordinate time at the geocentre. Given a common epoch of  $t_0 = 43144.0003725$  (Modified Julian Date), equations 9 and 10 relate measured TT to the IAU recommended coordinate timescales TCG (geocentric) and TCB (barycentric).

It should be noted that the time ephemeris of Irwin & Fukushima (1999) in fact takes its time argument,  $T_{\text{eph}}$ , in a reference frame that is a linear transformation of TCB, making the computation of the Einstein delay strictly an inverse problem. In practise, since the argument time scale has zero mean rate difference to TT, the latter can be substituted with negligible error in the result (Irwin & Fukushima 1999). In addition, the evaluation of equation (10) requires consulting the Solar system ephemeris (Section 2.5.3) which also takes  $T_{\text{eph}}$  times as its argument. Since  $T_{\text{eph}}$  is computed from TCB (equation 10), a circular dependency problem arises. This is solved to sufficient accuracy by two passes through an iterative refinement process.

### 2.5.2 Atmospheric Delays

The group velocity of radio waves in the atmosphere differs from the vacuum speed of light. Refractivity is induced both by the ionised fraction of the atmosphere (mainly in the ionosphere) and the neutral fraction (mainly in the troposphere).

The tropospheric propagation delay be separated into the so-called ‘‘hydrostatic’’ and ‘‘wet’’ components. In Very Long Baseline Interferometry (VLBI) and Global Positioning System (GPS) applications, these components are typically modelled as the product of the delay induced at the zenith, and a so-called ‘‘mapping function’’, which specifies the ratio between the zenith delay and the delay in a given direction. For a planar atmosphere, the mapping function is simply given by  $\text{csc } \Theta$  where  $\Theta$  is the source elevation angle. More advanced mapping functions take into account the curvature of the atmosphere, assuming azimuthal symmetry. The effect of azimuthal asymmetry is typically less than a nanosecond even at very low elevation angles (e.g. MacMillan 1995), and need not be considered for the present purpose.

The hydrostatic component contributes approximately 90% of the total delay, and may be computed a priori assuming a given mixture of gases in hydrostatic equilibrium. TEMPO2 uses the formula of Davis et al. (1985), re-written as a time delay

$$\Delta_{\text{hz}} = \frac{\left(\frac{P}{43.921 \text{ kPa}}\right)}{c \left[1 - 0.00266 \cos 2\varphi - \left(\frac{3.6 \times 10^6 \text{ m}}{H}\right)\right]}, \quad (11)$$

where  $\Delta_{\text{hz}}$  is the hydrostatic zenith delay,  $P$  is the surface atmospheric pressure,  $\varphi$  is the geodetic latitude of the site, and  $H$  is its height above the geoid. In combination with the mapping function, this leads to a timing term of amplitude  $\sim 7.7$  ns  $\cdot \text{csc } \Theta$ , mostly on a diurnal timescale. If atmospheric pressure data are unavailable, TEMPO2 uses a canonical value of one standard atmosphere (101.325 kPa). TEMPO2 uses the Niell Mapping Function (NMF; Niell 1996), which is of comparable accuracy to other published mapping functions but does not require meteorological data: it depends only on the source elevation.

The wet component of the tropospheric propagation delay is highly variable and cannot be predicted accurately. Fortunately, it is small. The zenith wet delay (ZWD;  $\Delta_{\text{wz}}$ ) may be measured using appropriate analyses of radiosonde, water vapour radiometer, GPS or VLBI observations (e.g. Niell et al. 2001), of which only GPS is likely to be obtainable on a routine basis at most radio observatories. If such measurements are available, TEMPO2 can make use of them in conjunction with the NMF to account for the effects of tropospheric water vapour on pulse times of arrival. The ZWD could conceivably be included as a free parameter in the pulsar timing model, but because the effect is small and varies from day to day, this would not be

possible with the sensitivity of presently attainable observing systems. For this reason, if no tabulated ZWD information is available, the effect is neglected.

Neglecting dispersion (below), the total atmospheric delay is written:

$$\Delta_A = m_h(\Theta)\Delta_{hz}(P) + m_w(\Theta)\Delta_{wz}(P), \quad (12)$$

where  $m_h(\Theta)$  and  $m_w(\Theta)$  are the Niell mapping functions for the hydrostatic and wet components. Values for  $P$  and  $\Delta_{wz}$  are to be provided as input data to TEMPO2, or default values of  $P = 101.325$  kPa and  $\Delta_{wz} = 0$  are used.

The passage of the signal through the ionosphere induces a dispersive delay that varies strongly with the Solar activity cycle and also on seasonal, diurnal and shorter timescales. The integrated column density of electrons (“total electron content”; TEC) in the ionosphere typically lies in the range 5–100 TECU (1 TECU =  $10^{16}$  m<sup>-2</sup>  $\simeq$   $3.2 \times 10^{-7}$  cm<sup>-3</sup> pc), corresponding to variable propagation delays of the order of 7–130 ns  $\cdot (f/1 \text{ GHz})^{-2}$ , where  $f$  is the observing frequency. Models of the ionosphere are available (e.g. Schaer 1999; Bilitza 2001), however the predicted TEC is accurate to only  $\sim$  3–20 TECU (Mamoru et al. 2003). In any case, ionospheric dispersion is inseparable from and smaller than uncertainties in interplanetary (Section 2.5.4) and interstellar (Section 2.6.1) dispersion, necessitating the inclusion of a fittable, fully time-variable dispersion parameter (Section 2.6.1).

### 2.5.3 Roemer delay and parallax

The Roemer delay is the simple vacuum delay between the arrival of the pulse at the observatory and the Solar system barycentre, not including effects related to the binary motion of, or finite distance to, the pulsar:

$$\Delta_{R\odot} = -\frac{\mathbf{r} \cdot \hat{\mathbf{R}}_{BB}}{c}, \quad (13)$$

where  $\hat{\mathbf{R}}_{BB} \equiv \mathbf{R}_{BB}/|\mathbf{R}_{BB}|$  is a unit vector in the direction of the binary barycentre at the time of observation. TEMPO2 performs this calculation in the BCRS.

The vector  $\hat{\mathbf{R}}_{BB}$  is constructed from the spherical coordinate angles of the ICRS source direction, right ascension ( $\alpha$ ) and declination ( $\delta$ ), at time  $t_{\text{pos}}$ , and the Cartesian components of the proper motion of the source in the plane of the sky ( $\mu_\alpha$  and  $\mu_\delta$ ) and along the line of sight ( $\mu_\parallel$ ), all of which are fittable parameters in TEMPO2:

$$\hat{\mathbf{R}}_{BB} = \hat{\mathbf{R}}_0 + \boldsymbol{\mu}_\perp (t_a^{\text{BB}} - t_{\text{pos}}) - \left(\frac{1}{2}|\boldsymbol{\mu}_\perp|^2 \hat{\mathbf{R}}_0 + \mu_\parallel \boldsymbol{\mu}_\perp\right) (t_a^{\text{BB}} - t_{\text{pos}})^2, \text{ where} \quad (14)$$

$$\hat{\mathbf{R}}_0 = \begin{pmatrix} \cos \alpha \cos \delta \\ \sin \alpha \cos \delta \\ \sin \delta \end{pmatrix} \quad (15)$$

$$\boldsymbol{\mu}_\perp = \mu_\alpha \hat{\boldsymbol{\alpha}} + \mu_\delta \hat{\boldsymbol{\delta}}, \quad (16)$$

$$\hat{\boldsymbol{\alpha}} = \begin{pmatrix} -\sin \alpha \\ \cos \alpha \\ 0 \end{pmatrix}, \text{ and} \quad (17)$$

$$\hat{\boldsymbol{\delta}} = \begin{pmatrix} -\cos \alpha \sin \delta \\ -\sin \alpha \sin \delta \\ \cos \delta \end{pmatrix}. \quad (18)$$

Alternatively, ecliptic coordinates ( $\lambda, \beta, \mu_\lambda, \mu_\beta$ ) may be used, in which case:

$$\hat{\mathbf{R}}_0 = \mathbf{E} \begin{pmatrix} \cos \lambda \cos \beta \\ \sin \lambda \cos \beta \\ \sin \beta \end{pmatrix}, \text{ and} \quad (19)$$

$$\boldsymbol{\mu}_\perp = \mu_\lambda \hat{\boldsymbol{\lambda}} + \mu_\beta \hat{\boldsymbol{\beta}}, \text{ where} \quad (20)$$

$$\mathbf{E} = \begin{pmatrix} 1 & 0 & 0 \\ 0 & \cos \epsilon_0 & -\sin \epsilon_0 \\ 0 & \sin \epsilon_0 & \cos \epsilon_0 \end{pmatrix}, \quad (21)$$

$$\hat{\boldsymbol{\lambda}} = \mathbf{E} \begin{pmatrix} -\sin \lambda \\ \cos \lambda \\ 0 \end{pmatrix}, \text{ and} \quad (22)$$

$$\hat{\boldsymbol{\beta}} = \mathbf{E} \begin{pmatrix} -\cos \lambda \sin \beta \\ -\sin \lambda \sin \beta \\ \cos \beta \end{pmatrix}. \quad (23)$$

Here  $\epsilon_0 = 84381.40578$  arcsec (Harada & Fukushima 2004) is the mean obliquity of the ecliptic at J2000.0.

The four terms that result from the expansion of equation (14) derive from corresponding terms in the expansion of equation (5), such that

$$\mathbf{r} \cdot \hat{\mathbf{R}}_{\text{BB}} = r_{\parallel} + \frac{\mathbf{k}_{\perp} \cdot \mathbf{r}_{\perp}}{|\mathbf{R}_0|} - \frac{r_{\parallel} |\mathbf{k}_{\perp}|^2}{2|\mathbf{R}_0|^2} - \frac{k_{\parallel} \mathbf{k}_{\perp} \cdot \mathbf{r}_{\perp}}{|\mathbf{R}_0|^2}. \quad (24)$$

Here we have assumed that  $\mathbf{k} = \mu |\mathbf{R}_0| (t_a^{\text{BB}} - t_{\text{pos}})$ , safely neglecting any acceleration or higher order secular motion of the pulsar or BB (Section 2.3). In principle,  $t_a^{\text{BB}}$  cannot be computed without first knowing  $\Delta_{\text{R}\odot}$ ; this is resolved by initially setting  $t_a^{\text{BB}}$  to the TCB time of arrival at the observatory, and iteratively refining  $\Delta_{\odot}$  and  $\Delta_{\text{IS}}$  until convergence.

Equation 24 consists of four terms corresponding to the expression in equation 14 of the instantaneous source direction as the sum of four contributions. These are the initial direction (yielding the first term of equation 24), the proper motion (second term), a correction to maintain unit length after addition of the proper motion (third term) and the acceleration or deceleration of the proper motion owing to the fact that over time, the proper motion moves the source vector, causing part of the initially radial velocity to acquire a transverse component (fourth term). The third term can also be interpreted as the proper-motion-induced second-order reduction in the projection of the source direction on the radial component of  $\mathbf{r}$  that accompanies the first-order increase in its projection upon the transverse component of  $\mathbf{r}$ . Another alternative interpretation of the third term is that it corrects the Shklovskii term (Section 2.6.2) for the distance variations induced by the Earth’s orbital motion. The fourth term, first introduced by N. Wex (1997, unpublished contribution to TEMPO), provides one of two possible ways of accessing the elusive radial velocity, the integrated first-order contribution of which ( $k_{\parallel}$ ) is otherwise inseparable from a Doppler shift of the pulse and orbital frequencies and their derivatives. The second method is described in Section 2.6.2.

The first term of equation (13) describes the difference in time of arrival of a pulse at the SSB compared to that at the point obtained by projecting the SSB–observatory vector on the SSB–BB vector. The arrival time at that point differs again from the arrival time at the observatory due to the curvature of spherical “wavefronts” connecting photons emitted simultaneously from the pulsar. This term is referred to as the “parallax” term, although it differs somewhat from stellar parallax: positional astrometry measures the three-dimensional orientation of the wavefront normal, whereas pulsar timing measures the position of the wavefront in its intersection with the ecliptic. To first order the curvature is proportional to the square of the lateral displacement of the observatory from the SSB–BB vector, yielding an excess delay corresponding to one of the terms of equation (5):

$$\Delta_{\text{p}} = \frac{|\mathbf{r}_{\perp}|^2}{2cd_p}, \quad (25)$$

Here the “parallax distance”,  $d_p$  is substituted for  $|\mathbf{R}_0|$  to allow this effect to be separated from others involving the source distance. The conventional “parallax”  $\Pi \equiv 1 \text{ AU}/d_p$ , being the angle subtended from the source by line of 1 AU in length at the SSB, is a fittable parameter in TEMPO2. Its value is specified in units of milliarcseconds, corresponding numerically to the reciprocal of the distance in kiloparsecs.

In computing the Roemer and parallax delays, the vector  $\mathbf{r}$  is constructed in two steps, from the SSB to the geocentre and from the geocentre to the observatory, i.e.  $\mathbf{r} = \mathbf{r}_{\oplus} + \mathbf{s}$ . The first part ( $\mathbf{r}_{\oplus}$ ) is accomplished with the aid of a numerical Solar system ephemeris. The current default ephemeris is DE405 (Standish 1998), which is aligned within a known uncertainty to the ICRS, but uses a time and length scale slightly different than the SI second and metre (Standish 1998). TEMPO2 uses the equations and constants of Irwin & Fukushima (1999) to appropriately transform the TCB site arrival time (Section 2.5.1) for input to the ephemeris (using an offset and scale), and appropriately scales the output vectors to SI units. It should be noted that the use of alternative ephemerides that require a different transformation procedure will introduce errors (see Section 3.5).

The second part of the observatory position vector,  $\mathbf{s}$ , is obtained by transformation of the terrestrial observatory coordinates into the GCRS (which to sufficient accuracy is equivalent to the BCRS). This is accomplished using an ITRS site position vector ( $\mathbf{s}_{\text{ITRS}}$ ) supplied to TEMPO2, transformed to the GCRS using algorithms consistent with the IAU 2000 Resolutions. The transformation proceeds as follows:

$$\mathbf{s} = \mathbf{Q}(t_a^{\text{obs}}) \mathbf{R}(t_a^{\text{obs}}) \mathbf{W}(t_a^{\text{obs}}) \mathbf{s}_{\text{ITRS}}, \quad (26)$$

where the matrices  $\mathbf{W}$ ,  $\mathbf{R}$  and  $\mathbf{Q}$  account for polar motion, Earth rotation, and the motion of the Earth spin axis in the ICRS. The latter term in turn consists of a product of a frame bias and the IAU2000B precession-nutation matrix (McCarthy & Luzum 2003). Details of the construction of these matrices are available in the IERS Conventions (McCarthy & Petit 2004) and in the documentation of the IAU Standards of Fundamental Astronomy (SOFA) software library<sup>4</sup> used by TEMPO2 to compute them. Polar motion and Earth rotation both exhibit unpredictable variations that must be corrected post facto using

<sup>4</sup> <http://www.iau-sofa.rl.ac.uk/>

measured parameters. TEMPO2 uses the “C04” series of Earth orientation parameters, provided by the IERS, as input to the SOFA routines.

For the purposes of transforming the observing frequency to the barycentric frame (Section 2.6.1), the time derivative of the Roemer delay is needed:

$$\frac{d\Delta_{R\odot}}{dt} = \frac{(\dot{\mathbf{r}}_{\oplus} + \dot{\mathbf{s}}) \cdot \hat{\mathbf{R}}_0}{c}, \quad (27)$$

where dots denote the time derivative and the effects of proper motion and parallax are negligible. The barycentric velocity of the geocentre,  $\dot{\mathbf{r}}_{\oplus}$ , is provided by the Solar system ephemeris. The barycentric velocity of the site is dominated by the velocity imparted by Earth rotation. This is calculated using

$$\dot{\mathbf{s}}_{\text{ITRS}} = (\omega_{\oplus} \mathbf{W}^{-1} \hat{\mathbf{z}}) \times \mathbf{s}_{\text{ITRS}}. \quad (28)$$

Here a unit North vector ( $\hat{\mathbf{z}}$ ) is transformed using the inverse polar motion matrix and multiplied by the instantaneous Earth angular rotation rate  $\omega_{\oplus}$ , to give the angular velocity of the Earth in the ITRS. The cross product of this with the site radius vector gives the tangential velocity, which is transformed to the GCRS in the same manner as  $\mathbf{s}$ . Of the neglected terms in this approximation, the largest is the precessional velocity, at a negligible  $\sim 10^{-13}c$ .

#### 2.5.4 Solar system dispersion

Radio signals encounter significant dispersion in the interplanetary medium, due to the electron content of the Solar wind. The electron distribution follows a roughly  $r^{-2}$  form consistent with spherical expansion (Issautier et al. 1998). Integrating along the line of sight yields a dispersion measure (DM):

$$\begin{aligned} \text{DM}_{\odot} &= \int_0^{\infty} n_0 \left( \frac{1 \text{ AU}}{r(s)} \right)^2 ds \\ &= n_0 (1 \text{ AU})^2 \frac{\rho}{|\mathbf{r}| \sin \rho}, \end{aligned} \quad (29)$$

$$(30)$$

where  $|\mathbf{r}|$  is the heliocentric radius of the observatory,  $\rho$  is the pulsar-Sun-observatory angle, and  $n_0$  is an overall scale parameter, which can be specified in TEMPO2 parameter files as NE1AU. (It should be noted that equation (30) is an approximation that ignores the effects on the dispersion relation due to the bulk plasma velocity and its variation along the line of sight. However, there are other much more significant sources of error as discussed below.) The default value for  $n_0$  is  $4 \text{ cm}^{-3}$ , consistent with recent measurements (Issautier et al. 1998; Issautier et al. 2001; Splaver et al. 2005) and significantly lower than the value of  $9.961 \text{ cm}^{-3}$  used by TEMPO. The computed dispersion measure is used to calculate the delay due to interplanetary dispersion:

$$\Delta_{\text{D}\odot} = \frac{\text{DM}_{\odot}}{2.410 \times 10^{-16} \text{ cm}^{-3} \text{ pc}} \cdot (f^{\text{SSB}})^{-2} \quad (31)$$

where  $f^{\text{SSB}}$  is the observing frequency transformed to the barycentric frame (see Section 2.6.1).

This correction is of limited accuracy. Recent studies of with the *Ulysses* spacecraft have revealed extraordinary complexity in the Solar wind. At Solar minimum, the electron density (scaled by  $r^2$ ) was found to show RMS temporal variations of 10–50%, depending on heliocentric latitude (Issautier et al. 1998), while at Solar maximum the mean electron density increased but was subject to very strong modulation (Issautier et al. 2001). The default correction of equation (31) is therefore uncertain within at least factor of two, corresponding to a minimum of 130 ns of error at  $f = 1 \text{ GHz}$  for a source located at an ecliptic pole, increasing to many microseconds for sources within a few degrees of the ecliptic.

Errors in the predicted Solar system dispersion delay are of concern not only because they add random noise to the timing residuals and fitted parameters, but also because a portion of the error term will exhibit annual periodicities that could corrupt the fitted pulsar position, proper motion and parallax (Splaver et al. 2005). It is also possible that other periodicities in this term could be misinterpreted as arising due to a planetary companion to the pulsar (Scherer et al. 1997, though see also Wolszczan et al. 2000). Previous attempts to improve the model have focussed on adding fittable degrees of freedom (e.g. Cognard et al. 1996; Splaver et al. 2005), however the complex behaviour seen in the *Ulysses* observations indicate that the only way to adequately remove the effect is to measure it directly using multi-frequency observations (see Section 2.6.1).

#### 2.5.5 Shapiro delay

The Shapiro delay accounts for the time delay caused by the passage of the pulse through curved spacetime. The total delay obtained by summing over all the bodies in the Solar system (Backer & Hellings 1986):

$$\Delta_{\text{S}\odot} = -2 \sum_j \frac{Gm_j}{c^3} \ln(\hat{\mathbf{R}} \cdot \mathbf{r}_j + |\mathbf{r}_j|) + \Delta_{\text{S}\odot 2} \quad (32)$$



where  $\hat{\mathbf{R}}$  is a unit vector in the direction of the pulsar,  $m_j$  is the mass of body  $j$ ,  $\mathbf{r}_j$  is a vector from body  $j$  to the telescope, and  $\Delta_{\text{S}\odot 2}$  is a second-order correction discussed below. The first term may be re-written in the following more convenient form:

$$\Delta_{\text{S}\odot} = - \sum_j \frac{2Gm_j}{c^3} \ln |r_j| (1 - \cos \psi_j) + \Delta_{\text{S}\odot 2}, \quad (33)$$

where  $\psi_j$  is the pulsar-telescope-object angle for the  $j$ -th object. TEMPO2 includes the first-order Shapiro delay for the Sun, Venus, Jupiter, Saturn, Uranus and Neptune.

For observations of sources very close to Solar system bodies, higher-order effects may become important. The largest of these is the geometrical excess path length due to gravitational light bending (Richter & Matzner 1983), which amounts to 9.1 ns for a ray with a trajectory grazing the Solar limb<sup>5</sup>. From the derivation of Hellings (1986), assuming general relativity and re-parameterising in terms of  $\psi$  for a very distant source, this term is given by

$$\Delta_{\text{S}\odot 2} = \frac{4G^2 m^2}{c^5 |r| \tan \psi \sin \psi} \quad (34)$$

$$\simeq \frac{4G^2 m^2}{c^5 |r| \psi^2}. \quad (35)$$

For pulsar timing purposes, only the geometric delay due to the Sun need be considered.

## 2.6 Propagation through interstellar space

The propagation time of the signal from the pulsar (or binary system barycentre) to the SSB is conveniently broken into three contributions: the vacuum propagation delay, i.e. the path length divided by the vacuum speed of light, and the excess delay due to dispersion and other frequency-dependent delays:

$$\Delta_{\text{IS}} = \Delta_{\text{VP}} + \Delta_{\text{ISD}} + \Delta_{\text{FDD}} + \Delta_{\text{ES}}. \quad (36)$$

The fourth term accounts for the special relativistic time dilation between the SSB reference frame and the binary reference frame.

### 2.6.1 Interstellar dispersion and other frequency-dependent delays

The interstellar dispersion delay enters the timing model under the standard relation:

$$\Delta_{\text{ISD}} = \frac{D}{(f_{\text{SSB}})^2}, \quad (37)$$

where  $D$  is the so-called dispersion constant, and  $f_{\text{SSB}}$  is the frequency of the radiation at the Solar system barycentre. The barycentric frequency differs from the frequency at the observatory, due to a simple Doppler shift ( $\sim 10^{-4}$  in magnitude) and a second-order relativistic correction ( $\sim 10^{-8}$ ), plus the effects of gravitational redshift ( $\sim 10^{-8}$ ). The first term is simply the time derivative of the Roemer delay (the ‘‘Roemer rate’’), while the sum of the latter two are is derivative of the Einstein delay (the ‘‘Einstein rate’’).

$$f_{\text{SSB}} = \left( 1 + \frac{d\Delta_{R\odot}}{dt} + \frac{d\Delta_{E\odot}}{dt} \right) f. \quad (38)$$

Although  $D$  is the directly measurable quantity of equation (37), it is customary to speak in terms of the inferred column density of electrons along the line of sight, i.e. the dispersion measure,  $\text{DM} = k_{\text{D}} D$ . The value of  $k_{\text{D}}$  used by TEMPO2 (and TEMPO) is  $k_{\text{D}} \equiv 2.410 \times 10^{-16} \text{ cm}^{-3} \text{ pc}$ ; see Paper I for further discussion.

Many pulsars exhibit temporal variation in the interstellar dispersion measure. TEMPO2 follows other software packages in modelling these variations by means of a Taylor series:

$$\text{DM} = \sum_{n \geq 0} \frac{\text{DM}^{(n)}}{n!} (t_a^{\text{SSB}} - t_{\text{D}})^n, \quad (39)$$

where  $\text{DM}^{(n)}$  is the (fittable)  $n$ -th derivative of the dispersion measure and  $t_{\text{D}}$  is a user-specified epoch.

This approach is limited to modelling variations of low to moderate complexity. At the level of accuracy demanded by current high precision timing campaigns, significant unmodelled variations will appear on short timescales, due to ionospheric

<sup>5</sup> Hellings (1986) quotes a figure of 36 ns, referring to the calculation of Richter & Matzner (1983). However, that calculation incurred an extra pair of factors of two, one due to the fact that the calculation referred to a round trip, and one due the fact that the reflector was located 1 AU past the sun, rather than being a very distant source.

(Section 2.5.2), interplanetary (Section 2.5.4) and interstellar electrons (Foster & Cordes 1990). An alternative and recommended course of action is to use the “stride fit” feature of TEMPO2 (Paper I), to fit a different dispersion measure to every group of simultaneous (or contemporaneous) multi-frequency arrival time measurements.

TEMPO2 also allows for the fitting of an additional frequency-dependent delay term:

$$\Delta_{\text{FDD}} = k_f (f^{\text{SSB}})^\zeta, \quad (40)$$

where  $k_f$  and  $\zeta$  define the scale and spectral index of the term. This term may be used in conjunction with the stride fit feature to model, for example, delays due to refraction in the interstellar medium (Foster & Cordes 1990) or deviations from the cold plasma dispersion law (Phillips & Wolszczan 1992).

### 2.6.2 Vacuum propagation delay

The vacuum propagation delay is affected by the distance to the pulsar and the variation of this with time. The full geometric distance was derived in Section 2.3. The first term from equation (5) to be assigned to  $\Delta_{\text{IS}}$ ,  $|\mathbf{R}_0|/c$ , is in fact not measurable to even remotely sufficient precision, but is constant and so can be dropped from the timing formula. A side effect of this is that epochs of measured pulse frequencies, times of periastrons, glitches and so on are in fact retarded by the initial light propagation time,  $c|\mathbf{R}_0|$ . The remaining parts assigned to the interstellar delay are as follows:

$$s_{\text{IS}} = k_{\parallel} + \frac{|\mathbf{k}_{\perp}|^2}{2|\mathbf{R}_0|} - \frac{k_{\parallel}|\mathbf{k}_{\perp}|^2}{2|\mathbf{R}_0|^2}. \quad (41)$$

The first term on the right hand side of equation (41) simply represents the displacement of the system in the initially radial direction. This receives potentially significant contributions from the radial velocity of the pulsar and the radial acceleration in the gravitational potential of the globular cluster or Galactic environment (Damour & Taylor 1991). The second term describes the so-called Shklovskii effect (Shklovskii 1970), whereby initially transverse motion attains a radial component due to the change in the direction of the line of sight caused by the transverse motion of the pulsar. That is, the pulsar moves tangentially while a path of constant distance describes a circle centred on the SSB. The distance between the two is the excess propagation length. The third term in corresponds to secular change in the size of the Shklovskii effect as the radial motion increases or decreases the distance, and hence changes the curvature of the line of constant distance just mentioned. An alternative interpretation of this term is that it is the cumulative effect upon the Shklovskii term caused by the increase or decrease in the apparent proper motion owing to the increasing transverse component of the initially radial motion (Section 2.5.3). To our knowledge, this effect was first noted by van Straten (2003), in the context of its manifestation as an apparent second derivative of the spin and orbital periods.

These effects are often neglected in timing formulae, because as simple constant or secularly increasing Doppler shifts, they are inseparable from the pulse and orbital periods and their derivatives. A common procedure is to correct the apparent period derivatives by estimating the contributions of transverse motion and gravitational acceleration and subtracting them to obtain the intrinsic value (e.g. Damour & Taylor 1991; Camilo et al. 1994). Alternatively, in certain binary systems where the true orbital period derivative is expected to be negligible, the measured derivative can be attributed entirely to these effects to obtain, in combination with a measurement of the transverse proper motion, an estimate of  $|\mathbf{R}_0|$  (Bell & Bailes 1996). Likewise, a measured second spin frequency derivative could, in principle, yield a measurement of the radial velocity (van Straten 2003) via the third term of equation (41).

As an alternative to modelling these effects via artificial contributions to spin and binary parameters, TEMPO2 can optionally include them directly in the following form:

$$\Delta_{\text{VP}} = \frac{v_{\parallel}}{c} (t_{\text{a}}^{\text{BB}} - t_{\text{pos}}) + \frac{a_{\parallel} + d_{\text{Shk}}|\boldsymbol{\mu}_{\perp}|^2}{2c} (t_{\text{a}}^{\text{BB}} - t_{\text{pos}})^2 + \frac{1}{2c} (a_{\mu} - v_{\parallel\text{Shkdot}}|\boldsymbol{\mu}_{\perp}|^2) (t_{\text{a}}^{\text{BB}} - t_{\text{pos}})^3, \quad (42)$$

where  $v_{\parallel\text{Shkdot}}$ ,  $a_{\parallel}$ ,  $d_{\text{Shk}}$  and  $a_{\mu} \equiv \mathbf{a}_{\perp} \cdot \boldsymbol{\mu}_{\perp}$  are fittable parameters that specify the radial velocity, radial acceleration, Shklovskii distance, and component of acceleration in the direction of the transverse proper motion. The terms involving acceleration arise due to the expansion of  $\mathbf{k}$  in terms of proper motion, distance and acceleration (equation 6). The circular dependence of  $\Delta_{\text{VP}}$  and  $t_{\text{a}}^{\text{BB}}$  is resolved by iteration as described in Section 2.5.3.

The parameters  $a_{\parallel}$  and  $d_{\text{Shk}}$  are inseparable, and highly covariant with a simultaneous change to the spin frequency derivative and orbital period derivative. It is therefore imperative that at least one of the first two parameters plus any one of the remaining three parameters are held fixed at some independently determined value when fitting. These parameters are included separately because each of them is potentially subject to external constraints. The transverse proper motion,  $\boldsymbol{\mu}_{\perp}$ , is typically immune from this covariance due to its appearance in the annual proper motion term (Section 2.5.3). Likewise,  $v_{\parallel\text{Shkdot}}$  and  $a_{\mu}$  are inseparable, and highly covariant with the spin frequency second derivative, so only one of these parameters should be allowed to vary in a fit. They are included separately because  $v_{\parallel}$  may be determined from  $\mu_{\parallel}$  (Section 2.5.3) and one or more of the distance parameters, while  $\mathbf{a}$  may be estimated from models of the Galactic rotation and gravitational potential. The first-order radial velocity term is discussed in the following section.

### 2.6.3 Transformation from SSB to BB coordinate time

The final term contributing to  $\Delta_{\text{IS}}$  accounts for the special relativistic time dilation owing to the relative velocities of the Solar system and binary barycentres:

$$t^{\text{BB}} - t_{\text{pos}} = \frac{t^{\text{SSB}} - t_{\text{pos}}}{\sqrt{1 - |\mathbf{v}|^2/c^2}}, \quad (43)$$

where  $\mathbf{v}$  is the relative velocity of the frames. This transformation is applied to the arrival time of the pulse at the BB, so that

$$t_{\text{a}}^{\text{BB}} = t_{\text{a}}^{\text{SSB}} - \Delta_{\text{ISD}} - \Delta_{\text{FDD}} - \Delta_{\text{VP}} - \Delta_{\text{ES}}, \quad \text{where} \quad (44)$$

$$\Delta_{\text{ES}} = \frac{v^2}{2c^2} (t_{\text{a}}^{\text{SSB}} - t_{\text{pos}} - \Delta_{\text{ISD}} - \Delta_{\text{FDD}} - \Delta_{\text{VP}}), \quad (45)$$

neglecting terms of order  $v^4/c^4$  and higher. Here the notation  $\Delta_{\text{ES}}$  refers to the fact that the term is analogous to the Solar system and binary Einstein delays (Sections 2.5.1 and 2.7.4) and relates to the relative secular motion of the SSB and BB.

This transformation combines with the much larger  $v_{\parallel}/c$  term of equation (42) to effect a Doppler shift between the two frames:

$$\Gamma = \frac{dt_{\text{a}}^{\text{SSB}}}{dt_{\text{a}}^{\text{BB}}} (t_{\text{a}}^{\text{SSB}} = t_{\text{pos}}) \quad (46)$$

$$= \frac{1 - v_{\parallel}/c}{\sqrt{1 - v^2/c^2}}. \quad (47)$$

An unknown Doppler shift of this kind cannot be distinguished from a re-scaling of various parameters intended to refer to the BB frame, meaning that neither  $v_{\parallel}$  nor  $v^2$  can be measured via their contribution to  $\Gamma$ . In fact, because the numerical values used for  $c$  and  $G$  are the same in all frames, the effect of neglecting  $\Delta_{\text{ES}}$  is the same as a change of unit system involving re-scaling of the length mass and time units, and physical tests involving only “measured” (wrong) parameters and these constants will remain valid (Damour & Deruelle 1986).

In the timing model presented here (and in contrast to that of Damour & Deruelle 1986),  $\mathbf{v}$  can in principle be deduced from parameters measured via other terms of equation (5). For this reason it may be included by specifying non-fittable values for the initial radial velocity  $v_{\parallel}$  and transverse speed  $v_{\perp}$  in the parameter file, which correct for the Doppler effect via equation (42) and the following formulation of the relativistic second-order Doppler shift:

$$\Delta_{\text{ES}} = \frac{v_{\parallel}^2 + v_{\perp}^2}{2c^2} (t_{\text{a}}^{\text{SSB}} - t_{\text{pos}} - \Delta_{\text{ISD}} - \Delta_{\text{FDD}} - \Delta_{\text{VP}}) \quad (48)$$

However, it must be remembered that in practice, the uncertainty of many parameters measured in the frame of the binary barycentre or pulsar will be dominated by the uncertainties in  $v_{\parallel}$  and  $v_{\perp}$ .

## 2.7 The effects of a binary companion

The effects of a binary companion are separated into several components: the geometric Roemer delay, which accounts for excess the vacuum light travel time due to the Euclidean displacement of the pulsar, a pseudo-delay that accounts for the aberration of the radio beam by binary motion, the Einstein delay (combined gravitational redshift and special relativistic time dilation in the pulsar frame) and Shapiro delay (gravitational time dilation in the vicinity of the companion):

$$\Delta_{\text{B}} = \Delta_{\text{RB}} + \Delta_{\text{AB}} + \Delta_{\text{EB}} + \Delta_{\text{SB}}. \quad (49)$$

The binary model used by TEMPO2 is based upon those of Blandford & Teukolsky (1976), Damour & Deruelle (1986; hereafter DD), Taylor & Weisberg (1989), Wex (1998 unpublished contribution to TEMPO; see also Lange et al. 2001) and Wex (1998), with extra terms as described by Kopeikin (1995, 1996).

### 2.7.1 Roemer delay and Kopeikin terms

The variation in the distance of the pulsar due to binary motion contributes four significant terms to the full geometric path length of equation (5):

$$s_{\text{B}} = b_{\parallel} + \frac{1}{|\mathbf{R}_{\text{0}}|} \left( \mathbf{k}_{\perp} \cdot \mathbf{b}_{\perp} - \mathbf{r}_{\perp} \cdot \mathbf{b}_{\perp} + \frac{|\mathbf{b}_{\perp}|^2}{2} \right). \quad (50)$$

The first term of equation (50) is the well-known first-order geometric delay due to the initially radial component of the displacement due to binary motion. The remaining terms are much smaller in magnitude and have only proven measurable in a few pulsars to date. Hereafter we shall refer to these collectively as the “Kopeikin terms”.

The second term of equation (50) describes changes to the apparent viewing geometry of the orbital motion, due to the proper motion of the system (Arzoumanian et al. 1996; Kopeikin 1996). An approach taken in the past to account for this effect is to allow it to be absorbed in derivatives of the projected semi-major axis,  $x$ , and longitude of periastron,  $\omega$ , with the measured values being converted into constraints on the position angle of ascending node,  $\Omega$ , and the inclination,  $i$  (e.g. Sandhu et al. 1997; Nice et al. 2001). Alternatively, the binary model can be modified to explicitly include linear changes to  $x$  and  $\omega$  as parameterised by fittable parameters  $\Omega$  and  $i$  (e.g. van Straten 2004). Here we take a third approach which we believe is cleaner: rather than defining the orbital parameters in a rotating reference frame, we state explicitly that the orbital parameters refer to the reference frame defined by the “initial” geometry at time  $t_{\text{BB}}$ , and hence account for the effect directly via the second term of equation (50).

The third term of equation (50) describes the so-called annual-orbital parallax (Kopeikin 1995). This may be interpreted either as the modulation of the Solar system Roemer delay (Section 2.5.3) due to the transverse orbital motion of the pulsar, or the modulation of the binary Roemer delay (first term of equation 50) due to the transverse orbital motion of the Earth. As with the secular changes to the apparent viewing geometry, although the annual-orbital parallax has been modelled in the past by perturbing the orbital parameters with terms involving  $\mathbf{r}$  (van Straten et al. 2001; Splaver et al. 2005), we choose maintain a consistent reference frame for the orbital parameters and instead model the effect directly via the third term of equation (50).

The fourth term of equation (50) is the orbital parallax (Kopeikin 1995), which accounts for the fact that transverse binary motion alters the line of sight and thereby acquires an apparently radial component: this is the orbital equivalent of the Shklovskii effect (Section 2.6.2). To our knowledge this is yet to be measured in any pulsar, and naturally cannot be absorbed in time-varying orbital parameters since the changes themselves occur on the orbital timescale.

The contributions of the four terms of equation (50) are included in the timing model as follows:

$$\Delta_{\text{RB}} = \Delta_{\text{RB}\parallel} + \Delta_{\text{KB}}, \text{ where} \quad (51)$$

$$\Delta_{\text{RB}\parallel} = \frac{b_{\parallel}}{c} \text{ and} \quad (52)$$

$$\Delta_{\text{KB}} = \frac{1}{c} (t_{\text{a}}^{\text{BB}} - t_{\text{pos}}) \boldsymbol{\mu}_{\perp\text{B}} \cdot \mathbf{b}_{\perp} - \frac{\mathbf{r}_{\perp} \cdot \mathbf{b}_{\perp}}{cd_{\text{AOP}}} + \frac{|\mathbf{b}_{\perp}|^2}{2cd_{\text{OP}}}. \quad (53)$$

where  $d_{\text{AOP}}$  and  $d_{\text{OP}}$  are estimates of the initial distance which can be either held fixed at some independently determined value (or omitted from the parameter file, to neglect the effect), tied to other fittable distance parameters (e.g.  $d_p$  and/or  $d_{\text{Shk}}$ ), or, given sufficient constraints on the relevant orbital parameters, fitted to obtain independent distance estimates. Likewise,  $\boldsymbol{\mu}_{\perp\text{B}}$  can be either tied to  $\boldsymbol{\mu}_{\perp}$ , or omitted from the parameter file to neglect the effect. Note that these parameters in fact refer to the quantities as observed in a frame that is comoving with the BB, in contrast to corresponding distance and proper motion parameters in preceding sections. However, the transformation can be neglected for a fractional error of  $O(v^2/c^2) < \sim 10^{-5}$  in those parameters, corresponding to changes in the time of emission calculation well below our 1-ns goal.

### 2.7.2 Post-Newtonian orbital kinematics

Calculation of the various orbital delays depends upon a knowledge of the displacement  $\mathbf{b}$  of the pulsar from the binary system barycentre, or at least its radial component  $b_{\parallel}$ , depending on the demanded accuracy. TEMPO2 follows the generalised post-Newtonian treatment of DD for the calculation of  $\mathbf{b}$ , with the addition of secular derivatives for the orbital period, eccentricity and projected semi-major axis after Taylor & Weisberg (1989). Specifically, from equations (16–17) of DD

$$\mathbf{b} = \begin{pmatrix} \hat{\mathbf{e}}_1 & \hat{\mathbf{e}}_2 & \hat{\mathbf{R}}_0 \end{pmatrix} \begin{pmatrix} \sin \Omega & -\cos \Omega & 0 \\ \cos \Omega & \sin \Omega & 0 \\ 0 & 0 & 1 \end{pmatrix} \begin{pmatrix} 1 & 0 & 0 \\ 0 & -\cos i & -\sin i \\ 0 & \sin i & -\cos i \end{pmatrix} \begin{pmatrix} |\mathbf{b}| \cos \theta \\ |\mathbf{b}| \sin \theta \\ 0 \end{pmatrix}, \text{ where} \quad (54)$$

$$|\mathbf{b}| = a(1 - e_r \cos u), \quad (55)$$

$$n(t_e^{\text{DSR}} - T_0) = u - e \sin u, \quad (56)$$

$$\theta = \omega + A_{e_{\theta}}(u), \quad (57)$$

$$A_e(u) = 2 \tan^{-1} \left[ \left( \frac{1+e}{1-e} \right)^2 \tan \frac{u}{2} \right], \quad (58)$$

$$e_r = e(1 + \delta_r) \quad (59)$$

$$e_{\theta} = e(1 + \delta_{\theta}) \quad (60)$$

$$n = \frac{2\pi}{P_{b0}} + \frac{\pi \dot{P}_b (t_e^{\text{DSR}} - T_0)}{P_{b0}^2}, \quad (61)$$

$$\omega = \omega_0 + kA_e(u), \quad (62)$$

$$k = \frac{\dot{\omega}}{n}, \quad (63)$$

$$e = e_0 + \dot{e}(t_e^{\text{psr}} - T_0), \quad (64)$$

where  $P_{b0}$  and  $\dot{P}_b$  are the initial value of the orbital period and its derivative,  $\omega_0$  and  $\dot{\omega}$  are initial longitude of periastron and the mean of its derivative,  $T_0$  is the proper time of periastron,  $e_0$  and  $\dot{e}$  are the initial ‘‘proper time eccentricity’’ and its derivative, and  $\delta_r$  and  $\delta_\theta$  parameterise relativistic deformations of the orbit. The matrices of equation (54) in right-to-left order account for the inclination of the orbit to the line of sight ( $i$ ), rotation about the line of sight ( $\Omega$ ), and projection from a radial–transverse basis to a frame rotationally aligned to the ICRS (Section 2.2). The matrices are chosen such that for  $i = 0$ , the angular momentum vector of the orbit is antiparallel to  $\hat{\mathbf{R}}_0$ , and  $\Omega$  measures the position angle of the ascending node with respect to  $\hat{\mathbf{e}}_2$ , in the sense of rotation into  $\hat{\mathbf{e}}_1$ . The definitions of  $i$  and  $\Omega$  therefore correspond to astronomical convention if  $\hat{\mathbf{e}}_1$  and  $\hat{\mathbf{e}}_2$  are east and north vectors. This is the case by default in TEMPO2:  $\hat{\mathbf{e}}_1 = \hat{\boldsymbol{\alpha}}$ ,  $\hat{\mathbf{e}}_2 = \hat{\boldsymbol{\delta}}$ . Alternatively, if ecliptic coordinates are in use (Section 2.5.3),  $\hat{\mathbf{e}}_1 = \hat{\boldsymbol{\lambda}}$  and  $\hat{\mathbf{e}}_2 = \hat{\boldsymbol{\beta}}$ , so that position angles are measured counter-clockwise from an ecliptic meridian.

Note that the solution to Kepler’s equation (56) involves the proper time of emission,  $t_e^{\text{psr}}$ . This depends upon the equivalent coordinate time of arrival at the BB, which in turn is related to the proper time of reception at the observatory by all of the terms in the timing model, including those involving  $t_e^{\text{psr}}$ . This circular dependence is resolved by starting with  $t_{\text{psr}}^e = t_a^{\text{BB}}$ , computing the orbital delays, making an updated estimate of  $t_{\text{psr}}^e$ , and iterating this process until the change in the orbital delay is less than 100 ps.

Using the above expression for  $\mathbf{b}$  and writing it in terms of its transverse and radial components, the geometric delay of equation (51) can be found explicitly. Beginning by expanding  $S \equiv |\mathbf{b}|/a \sin \theta$  and  $C \equiv |\mathbf{b}|/a \cos \theta$ ,

$$S = \sin \omega (\cos u - e_r) + \cos \omega (1 - e_\theta^2)^{1/2} \sin u, \text{ and} \quad (65)$$

$$C = \cos \omega (\cos u - e_r) - \sin \omega (1 - e_\theta^2)^{1/2} \sin u, \quad (66)$$

where we have followed the Appendix of DD in making a minor modification to the definition of  $e$  to simplify the expressions. Writing equation (54) in terms of the projections of  $\mathbf{b}$  upon  $\hat{\mathbf{e}}_1$ ,  $\hat{\mathbf{e}}_2$  and  $\hat{\mathbf{R}}_0$  as a function of  $S$  and  $C$ ,

$$b_1 = a(C \sin \Omega + S \cos \Omega \cos i), \quad (67)$$

$$b_2 = a(C \cos \Omega - S \sin \Omega \cos i), \text{ and} \quad (68)$$

$$b_{\parallel} = aS \sin i. \quad (69)$$

The basic Roemer delay may then be written:

$$\Delta_{\text{RB}\parallel} = xS, \text{ where} \quad (70)$$

$$x = x_0 + \dot{x}(t_e^{\text{psr}} - T_0), \quad (71)$$

and  $x \equiv a/c \sin i$  is the projected semi-major axis as a vacuum light travel time, defined in terms of its initial value,  $x_0$  (DD) and its derivative,  $\dot{x}$  (Taylor & Weisberg 1989). For the Kopeikin terms, following equation 53,

$$\Delta_{\text{KB}} = \Delta_{\text{SR}} + \Delta_{\text{AOP}} + \Delta_{\text{OP}}, \text{ where} \quad (72)$$

$$\Delta_{\text{SR}} = x(t_a^{\text{BB}} - t_{\text{pos}}) [(\mu_1 \sin \Omega + \mu_2 \cos \Omega)C \csc i + (\mu_1 \cos \Omega - \mu_2 \sin \Omega)S \cot i], \quad (73)$$

$$\Delta_{\text{AOP}} = -\frac{x}{d_{\text{AOP}}} [(r \cdot \hat{\mathbf{e}}_1 \sin \Omega + r \cdot \hat{\mathbf{e}}_2 \cos \Omega)C \csc i + (r \cdot \hat{\mathbf{e}}_1 \cos \Omega - r \cdot \hat{\mathbf{e}}_2 \sin \Omega)S \cot i], \text{ and} \quad (74)$$

$$\Delta_{\text{OP}} = \frac{cx^2}{2d_{\text{OP}}} (C^2 \csc^2 i + S^2 \cot^2 i). \quad (75)$$

The proper motion components are defined in terms of fittable parameters that can optionally float independently to the annual proper motion parameters (Section 2.5.3), in order to allow the latter to be separated from the secular change of binary viewing geometry. For equatorial coordinates,  $\mu_1 = \mu_{\alpha\text{B}}$  and  $\mu_2 = \mu_{\delta\text{B}}$ , while for ecliptic coordinates  $\mu_1 = \mu_{\lambda\text{B}}$  and  $\mu_2 = \mu_{\beta\text{B}}$ . In agreement with astronomical convention, the parameter  $\Omega$  corresponds to the position angle of periastron in terms of eastward rotation from north, while the parameter  $i$  is defined such that  $i = 0$  corresponds to a binary orbital angular momentum vector directed towards the observer. As pointed out by Splaver et al. (2005), these differ from the definitions of Kopeikin (1995, 1996). We note that some caution is required in this area owing to variations in definitions in the literature: for other examples of use of the unconventional definition of  $i$  see e.g. DD; Damour & Taylor (1992); Weisberg & Taylor (2002); Stairs et al. (2004).

### 2.7.3 Aberration

Owing to the relative transverse velocity of the pulsar and the Earth, the direction of the observer as seen from the pulsar differs from that which would be measured in a frame co-moving with the observer. The direction is aberrated according

to the Lorentz transformation that relates the two frames. Under the assumption that the source of pulses is the periodic rotation of an emission beam, any such change in the direction of the observer alters the rotational phase corresponding to radiation received at a given time. Following DD (equation 27), in TEMPO2 this is converted to an equivalent time delay:

$$\Delta_{\text{AB}} = A \{ \sin[\omega + A_e(u)] + e \sin \omega \} + B \{ \cos[\omega + A_e(u)] + e \cos \omega \}, \quad (76)$$

where  $A$  and  $B$  are parameters related to the orientation of the pulsar spin axis and the size of the orbit (see DD equations 38–39 and DD section 3.2). As discussed by DD, these parameters are highly covariant with the other binary parameters, and may only be separated on the time scale of geodetic precession. Note, here the relative motion of the observatory and the BB is neglected.

#### 2.7.4 Post-Newtonian delays

In addition to the modified Roemer delay of equation (51) and the aberration pseudo-delay, under the post-Keplerian formalism of DD there are two additional delay terms: the Einstein delay and the Shapiro delay.

The Einstein delay is the difference between the proper time of emission and the coordinate time in the quasi-inertial frame of the binary barycentre:

$$t^{\text{BB}} = t^{\text{psr}} + \Delta_{\text{EB}}. \quad (77)$$

This is due to the combined effect of gravitational redshift and time dilation. Following DD and in contrast to the TEMPO2 treatment of the Solar system Einstein delay, the binary Einstein delay specifically excludes a linear term by scaling  $t^{\text{psr}}$  in such a way that the orbital period is numerically the same in either time scale. It is expressed in a theory-independent manner in terms of a timing model parameter,  $\gamma$ ; from equation (19) of DD:

$$\Delta_{\text{EB}} = \gamma \sin u. \quad (78)$$

The Shapiro delay is caused by the curvature of space-time in the gravitational field of the binary companion. After equation (26) of DD:

$$\Delta_{\text{SB}} = -2r \log \left\{ 1 - e \cos u - s \left[ \sin \omega (\cos u - e) + (1 - e^2)^{1/2} \cos \omega \sin u \right] \right\}. \quad (79)$$

Here the fittable parameters are the theory-independent “range”,  $r$ , and “shape”,  $s$ . Under general relativity,  $s = \sin i$  and  $r = Gm_2/c^3$ , where  $m_2$  is the mass of the binary companion. In TEMPO2,  $r$  is expressed in units of  $T_\odot = GM_\odot/c^3$ , so that its value is numerically equal to the GR companion mass in units solar masses. ( $T_\odot$  is half the light travel time across the Solar Schwarzschild radius.) An alternative parameterisation is available, where the parameter  $s$  is replaced by the “SHAPMAX” parameter,  $z_s \equiv -\ln(1 - s)$ , This derives from a modification to TEMPO designed to avoid difficulties in fitting highly inclined orbits near  $|\sin i| = 1$  (Kramer et al. 2006a). In this case, the above relation applies after substituting  $s = 1 - \exp(-z_s)$ .

#### 2.7.5 Assuming general relativity

The post-Keplerian parameters of Sections 2.7.2 and 2.7.4 ( $\dot{P}_b, \dot{\omega}, \delta_r, \delta_\theta, \gamma, s, m_2$ ) can either be specified directly, or they can be derived from a reduced set of physical parameters based on the assumption that the predictions made by general relativity are correct. These parameters are  $m_2$  and  $M \equiv m_1 + m_2$ , the total system mass (in addition to the Keplerian parameters,  $P_{b0}, \omega_0, e, T_0$ , and  $x_0$ ). After equations 8.48–8.55 of Lorimer & Kramer (2005),

$$\dot{\omega}^{\text{GR}} = 3T_\odot^{2/3} n^{5/3} \frac{M^{2/3}}{1 - e^2}, \quad (80)$$

$$\gamma^{\text{GR}} = T_\odot^{2/3} n^{-1/3} e \frac{m_2(m_1 + 2m_2)}{M^{4/3}}, \quad (81)$$

$$r^{\text{GR}} = T_\odot m_2, \quad (82)$$

$$s^{\text{GR}} = \sin i = T_\odot^{-1/3} n^{2/3} x \frac{M^{2/3}}{m_2}, \quad (83)$$

$$\delta_r^{\text{GR}} = T_\odot^{2/3} n^{2/3} \frac{3m_1^2 + 6m_1m_2 + 2m_2^2}{M^{4/3}}, \quad (84)$$

$$\delta_\theta^{\text{GR}} = T_\odot^{2/3} n^{2/3} \frac{\frac{7}{2}m_1^2 + 6m_1m_2 + 2m_2^2}{M^{4/3}}, \text{ and} \quad (85)$$

$$\dot{P}_b^{\text{GR}} = -\frac{192\pi}{5} T_\odot^{5/3} n^{5/3} \frac{m_1m_2}{M^{1/3}} \frac{1 + 73e^2/24 + 37e^4/96}{(1 - e^2)^{7/2}}. \quad (86)$$

Although these equations account fully for the general relativistic rates of change of orbital period and longitude of

periastron, extra variation in these parameters is allowed for via the parameters  $\dot{P}_{bx}$  and  $\dot{\omega}_x$ :

$$n^{\text{GR}} = \frac{2\pi}{P_{b0}} + \frac{\pi (\dot{P}_b^{\text{GR}} + \dot{P}_{bx}) (t_e^{\text{psr}} - T_0)}{P_{b0}^2} \text{ and} \quad (87)$$

$$\omega^{\text{GR}} = \omega_0 + \left( k^{\text{GR}} + \frac{\dot{\omega}_x}{n} \right) A_e(u). \quad (88)$$

Note that  $\dot{\omega}_x$  is not intended to model the secular change in orbital viewing geometry due to proper motion: this is modeled by a separate term in the timing model, causing  $\omega$  to be defined in a consistent, non-rotating reference frame (Section 2.7.1).

Under the condensed parameterisation of this section, the orientation of the spin axis may be separated from the orientation of the orbit normal vector to yield a physical parameterisation of the aberration delay (DD). Following equations 8.56–8.57 of Lorimer & Kramer (2005):

$$A^{\text{GR}} = \frac{T_\odot^{-1/3}}{(2\pi)^{2/3}} \frac{m_2}{\nu P_b^{1/3} (1 - e^2)^{1/2} M^{2/3}} \sin \chi \csc \xi, \quad (89)$$

$$B^{\text{GR}} = -\frac{T_\odot^{-1/3}}{(2\pi)^{2/3}} \frac{m_2}{\nu P_b^{1/3} (1 - e^2)^{1/2} M^{2/3}} \cos i \cos \chi \csc \xi, \quad (90)$$

where  $\nu$  is the pulsar spin frequency (Section 2.8),  $\xi$  is the inclination of the pulsar spin axis, and  $\chi$  is its position angle<sup>6</sup>, relative to the position angle of ascending node,  $\Omega$ . Here  $\chi$  and  $\csc \xi$  are the fittable parameters. Note that because  $\cos i$  is only ambiguously constrained by the Shapiro delay term ( $\cos i = \pm \sqrt{1 - \sin^2 i}$ ),  $\chi$  too is subject to ambiguity. To evaluate equation (90), TEMPO2 assumes that  $\cos i \geq 0$ . Values of  $\chi$  determined on this basis are therefore indistinguishable under the transformation  $\chi \rightarrow \pi - \chi$ . Only if  $i$  is measurable via the Kopeikin terms can this degeneracy be broken. A second, unbreakable degeneracy exists due to the fact that aberration is only sensitive to the projection of the transverse orbital velocity upon the spin axis:  $\xi \rightarrow \pi - \xi$ .

### 2.7.6 Nearly circular orbits

For low-eccentricity orbits,  $\omega$  and  $T_0$  are highly covariant, which complicates the analysis of the uncertainty in these parameters. This problem can be avoided by parameterising the motion in terms of the Laplace-Lagrange parameters,

$$\eta \equiv e \sin \omega \text{ and} \quad (91)$$

$$\kappa \equiv e \cos \omega, \quad (92)$$

and the time of ascending node,

$$T_{\text{asc}} \equiv T_0 - \omega/n \quad (93)$$

(Wex 1998 unpublished contribution to TEMPO as “ELL1” binary model). Following Lange et al. (2001), the following approximation to equation (70) applies, to order  $e$ :

$$\Delta_{RB\parallel}^{\text{LL}} = x^{\text{LL}} S^{\text{LL}}, \text{ where} \quad (94)$$

$$S^{\text{LL}} = \sin \Phi + \frac{\kappa}{2} \sin 2\Phi - \frac{\eta}{2} \cos 2\Phi, \quad (95)$$

$$\Phi = n(t_e^{\text{psr}} - T_{\text{asc}}), \quad (96)$$

$$x^{\text{LL}} = x_0 + \dot{x}(t_e^{\text{psr}} - T_{\text{asc}}), \quad (97)$$

$$\eta = \eta_0 + \dot{\eta}(t_e^{\text{psr}} - T_{\text{asc}}), \text{ and} \quad (98)$$

$$\kappa = \kappa_0 + \dot{\kappa}(t_e^{\text{psr}} - T_{\text{asc}}). \quad (99)$$

Here  $\eta_0$ ,  $\dot{\eta}$ ,  $\kappa_0$ ,  $\dot{\kappa}$  and  $T_{\text{asc}}$  replace  $e_0$ ,  $\dot{e}$ ,  $\omega_0$ ,  $\dot{\omega}$  and  $T_0$  as fittable parameters, while  $\delta_\theta$  and  $\delta_r$  are neglected.

The original ELL1 model as presented by Lange et al. (2001) did not include the Kopeikin terms (Section 2.7.1). In order to include them, an expression for  $C$  (equation 66) is required. To the same accuracy as equation (95), we find

$$C^{\text{LL}} = \cos \Phi + \frac{\kappa}{2} \cos 2\Phi + \frac{\eta}{2} \sin 2\Phi, \quad (100)$$

neglecting a constant offset of  $3a\kappa/2$  (analogous to an offset of  $3x\eta/2$  dropped by Lange et al. 2001). Substitution into equations (73), (74) and (75) yields the Kopeikin terms under this parameterisation.

Under the Laplace-Lagrange parameterisation, the Shapiro delay is computed as follows (Lange et al. 2001):

<sup>6</sup> These are related to the  $\eta$  and  $\lambda$  of Damour & Taylor (1992) and Lorimer & Kramer (2005) via  $\chi = -\eta$ ,  $\xi = \pi - \lambda$ . The difference is to ensure the use of the conventional definition of position angle and inclination, see Section 2.7.2.

$$\Delta_{\text{SB}}^{\text{LL}} = -\frac{2Gm_2}{c^3} \ln(1 - \sin i \sin \Phi), \quad (101)$$

where either of the parameterisations ( $s$ ,  $z_s$ ) of  $\sin i$  of Section 2.7.4 may be used.

The aberration delay becomes (Wex 1998 unpublished):

$$\Delta_{\text{AB}}^{\text{LL}} = A \sin \Phi + B \cos \Phi. \quad (102)$$

The Einstein delay is neglected if this parameterisation is chosen.

### 2.7.7 Main sequence companions

The orbits of pulsars with main sequence binary companions show deviations from a Keplerian orbit attributed to spin-orbit coupling (Lai et al. 1995). TEMPO includes two binary models for taking these into account: the BTJ model, which induces steps (“jumps”) in several parameters at specified epochs (typically, at each periastron), and the MSS model, which includes orbital and secular variations to the inclination angle (Wex 1998). The insertion of jumps is straightforward and need not be discussed further. The MSS model is included in the TEMPO2 model by changing the manner in which  $\dot{x}$  alters  $x$ , and including second period derivatives in  $x$  and  $\omega$ :

$$x^{\text{MSS}} = x_0 + \frac{\dot{x}A_e(u)}{n} + \frac{\ddot{x}(t^{\text{psr}} - T_0)^2}{2}, \text{ and} \quad (103)$$

$$\omega^{\text{MSS}} = \omega_0 + kA_e(u) + \frac{\ddot{\omega}(t^{\text{psr}} - T_0)^2}{2}. \quad (104)$$

### 2.7.8 Emulating other models

As noted in Section 2.7.2, the orbital kinematics represent an inverse problem, because the motion is parameterised by the pulsar proper time, which itself depends on the orbital propagation delay. The standard approach in TEMPO2 is to iterate until convergence. However, in order to reproduce results from the implementations of the Blandford & Teukolsky (1976) or DD models, a facility is provided to alter this behaviour. Both of these models begin with the zeroth-order approximation that  $t_e^{\text{psr}} = t_a^{\text{BB}}$  to compute the various delay terms, then add correction terms to the zeroth-order approximation to the combined Roemer and Einstein delay,  $\Delta_{\text{RE}}^0$ , which is expressed (after DD equations 46–48) as follows:

$$\Delta_{\text{RE}}^0 = \alpha_{\text{B}}(\cos U - e_r) + (\beta + \gamma) \sin U, \text{ where} \quad (105)$$

$$\alpha_{\text{B}} = \frac{a \sin i}{c} \sin \omega, \quad (106)$$

$$\beta = \frac{a \sin i}{c} (1 - e_\theta^2)^{1/2} \cos \omega, \text{ and} \quad (107)$$

$$U - e_{\text{T}} \sin U = n(t^{\text{BB}} - T_0). \quad (108)$$

Note that the Kopeikin terms (equation 53) are neglected.

The expansion provided by DD is

$$\Delta_{\text{RE}}^{\text{DD}} = \Delta_{\text{RE}}^0 \left[ 1 - \hat{n} \Delta_{\text{RE}}^{0'} + \hat{n}^2 \left( \Delta_{\text{RE}}^{0'} \right)^2 + \frac{1}{2} \hat{n}^2 \Delta_{\text{RE}}^0 \Delta_{\text{RE}}^{0''} - \frac{1}{2} \frac{e \sin U}{1 - e \cos U} \hat{n}^2 \Delta_{\text{RE}}^0 \Delta_{\text{RE}}^{0''} \right], \text{ where} \quad (109)$$

$$\hat{n} = \frac{n}{1 - e \cos U}, \quad (110)$$

$$\Delta_{\text{RE}}^{0'} = -\alpha_{\text{B}} \sin U + (\beta + \gamma) \cos U, \text{ and} \quad (111)$$

$$\Delta_{\text{RE}}^{0''} = -\alpha_{\text{B}} \cos U - (\beta + \gamma) \sin U. \quad (112)$$

The approximation provided by Blandford & Teukolsky (1976) is equivalent to:

$$\Delta_{\text{RE}}^{\text{BT}} = \Delta_{\text{RE}}^0 \left( 1 - \hat{n} \Delta_{\text{RE}}^{0'} \right). \quad (113)$$

In addition, Blandford & Teukolsky (1976) neglected  $\Delta_{\text{BS}}$ ,  $\Delta_{\text{BA}}$ ,  $\delta_r$  and  $\delta_\theta$ , and the orbital modulation of  $\omega$ : that is, in contrast to equation (62),

$$\theta^{\text{BT}} = \omega_0 + \dot{\omega} (t^{\text{psr}} - T_0). \quad (114)$$

Keeping the DD formulation of  $\omega$  but the BT formulation of the other terms allows for the emulation of the BT+ model of TEMPO (Damour & Taylor 1992).

Additionally, it is possible to emulate the TEMPO implementation of the Laplace-Lagrange parameterisation (Section



2.7.6), which made an approximation to the Roemer delay analogous to the DD treatment:

$$\Delta_{\text{RB}}^{\text{ELL1}} = \Delta_{\text{RB}}^{\text{ELL1-0}} \left[ 1 - n\Delta_{\text{RB}}^{\text{ELL1-0}'} + \left( n\Delta_{\text{RB}}^{\text{ELL1-0}'} \right)^2 + \frac{1}{2}n^2\Delta_{\text{RB}}^{\text{ELL1-0}}\Delta_{\text{RB}}^{\text{ELL1-0}''} \right], \text{ where} \quad (115)$$

$$\Delta_{\text{RB}}^{\text{ELL1-0}} = \frac{x}{c} \left( \sin \Phi^0 + \frac{\kappa}{2} \sin 2\Phi^0 - \frac{\eta}{2} \cos 2\Phi \right), \quad (116)$$

$$\Delta_{\text{RB}}^{\text{ELL1-0}'} = x \cos \Phi, \quad (117)$$

$$\Delta_{\text{RB}}^{\text{ELL1-0}''} = -c \sin \Phi, \text{ and} \quad (118)$$

$$\Phi^0 = n(t_e^{\text{BB}} - T_{\text{asc}}). \quad (119)$$

## 2.8 Pulse phase model

The final component of the timing model is the evolution of the phase of the pulse sequence, relative to the proper time  $t^{\text{psr}}$  of the pulsar centre of mass (equation 7). In most cases, a simple Taylor series expansion is used:

$$\phi(t) = \sum_{n \geq 1} \frac{\nu^{(n-1)}}{n!} (t_e^{\text{psr}} - t_{\text{P}})^n + \phi_0. \quad (120)$$

The frequency derivative terms ( $\nu^{(n)}$ ) are the fittable parameters, while the epoch,  $t_{\text{P}}$ , at which  $\dot{\phi} = \nu$  is set by the user. Absolute phase alignment is achieved by means of  $\phi_0$ , which is not specified directly. Instead, in order to protect against changes in  $t_{\text{P}}$  or the choice of barycentric time scale,  $\phi_0$  is defined in terms of a reference time of arrival for a specified observing site and observing frequency. This time of arrival is chosen such that it is close to the centre of the time span of the fitted data, and has a predicted pulse phase that is exactly integer.

Note that under the assumption that the basic pulse train is a result of a rotating emission beam, the time of zero phase is in fact dependent on the position of the observer. Of all the sources of relative motion (Earth orbital, binary orbital and secular motion and acceleration), only the secular motion of the pulsar (or binary barycentre) is significant given our accuracy goal of 1 ns. However, since the transverse speed is nearly constant, so is the rate of change of apparent pulse phase, meaning that the effect cannot be separated from the basic pulse frequency,  $\nu$ . For this reason, the effect is neglected in TEMPO2. Likewise, the emitted beam is subject to aberration due to the relative velocity of the pulsar, however the constant component of this velocity contributes only a constant phase shift that is absorbed in  $\phi_0$ . On the other hand, the binary motion induces a variable aberration, which for simplicity is included in  $\Delta_B$  as a pseudo-propagation delay  $\Delta_A$  (Section 2.7.1).

Though the pulse frequency of most pulsars shows a continual gradual slow-down, attributed to magnetic braking of a spinning neutron star, certain pulsars exhibit anomalies known as ‘‘glitches’’. These events are generally well-modelled by permanent increments to the phase, frequency and frequency first derivative, in addition to a frequency increment that later decays exponentially to zero:

$$\phi_g = \begin{cases} \Delta\phi + \Delta\nu(t_e^{\text{psr}} - t_g) + \frac{1}{2}\Delta\dot{\nu}(t_e^{\text{psr}} - t_g)^2 + \left(1 - e^{-(t_e^{\text{psr}} - t_g)/\tau}\right) \Delta\nu_t(t_e^{\text{psr}} - t_g) & t_e^{\text{psr}} \geq t_g \\ 0 & t_e^{\text{psr}} < t_g. \end{cases} \quad (121)$$

An arbitrary number of glitches may be modelled in this manner, the corresponding values of  $\phi_g$  being added to the basic Taylor series of equation (120) to give the predicted evolution of pulse phase with time.

## 3 ACCURACY ESTIMATES

### 3.1 Geometric propagation delay

Errors are introduced to the geometric part of the propagation delay in two ways: through the neglect of various terms of equation (5), and through approximations made in the computation of other terms. Cases of the latter are discussed below. The neglected terms are the  $O(|\mathbf{R}_0|^{-3})$  terms, and all those involving the expansion of the third, second, and fourth terms in the second set of parentheses, except for the secular and annual changes to the Shklovskii effect and the secular change to the annual proper motion. Based upon measured parameters and a timing campaign spanning 20 years, we have estimated the likely magnitude of the neglected terms for all pulsars in the current ATNF pulsar catalogue having spin periods shorter than 30 ms (slower pulsars being unlikely to yield high precision timing measurements). The largest of the neglected terms are the change in annual proper motion due to transverse acceleration ( $\sim 1$  ns for PSR B1620–26), second-order secular changes to the apparent binary orbital viewing geometry ( $\sim 600$  ps for PSR J0437–4715), the  $O(|\mathbf{R}_0|^{-3})$  terms involving secular motion ( $\sim 600$  ps for PSR B1257+12), the binary modulation of the Shklovskii effect ( $\sim 300$  ps for PSR J0437–4715) and the second-order annual proper motion ( $\sim 100$  ps for PSR J0437–4715).

It is possible that pulsars yet to be discovered may yield larger errors than the examples listed here, if they are in wider

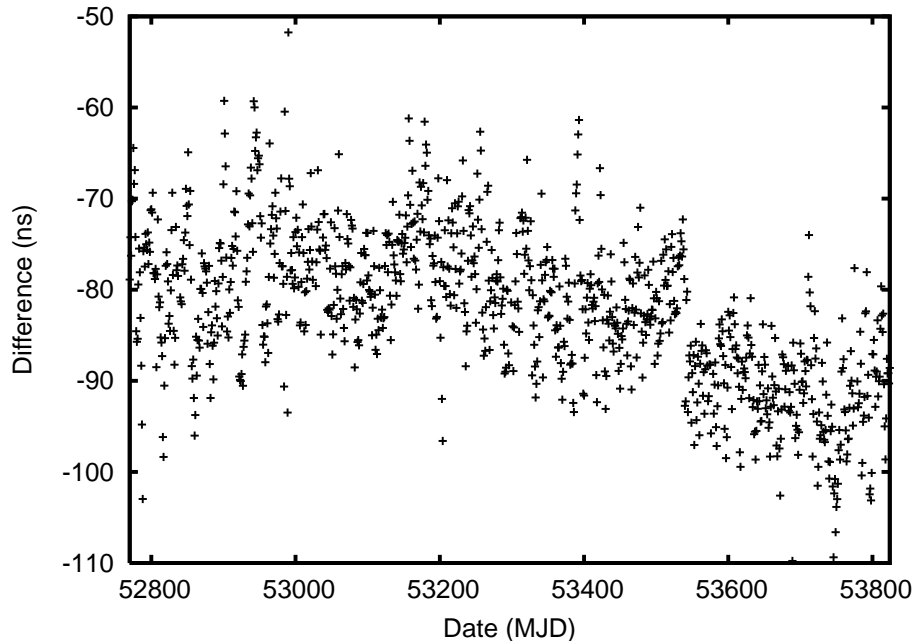


**Figure 1.** Round-trip time transfer error involving independent clock monitoring systems at Parkes observatory. The terms in each correction are UTC(GPS)–UTC(PKS) (“Totally Accurate Clock” system), UTC–UTC(GPS) (Circular T), UTC–UTC(AUS) (Circular T) and UTC(AUS)–UTC(PKS) (GPS common view system).

binary orbits, are closer to the Earth, have larger proper motions, and/or experience greater secular acceleration. The current sample is not likely to be biased in relation to proper motion, and any bias in relation to distance will tend to select closer pulsars due to the dependence of detection upon flux density. Highly accelerated pulsars are difficult to detect, however the level of acceleration at which this becomes problematic is many orders of magnitude larger than may be experienced in the Galactic or intracluster environment. Binary acceleration also hampers detection, but for the known population the lack of any strong dependence of companion mass upon orbital separation means that this selection effect biases the sample towards large orbital separations rather than small. However, it is not inconceivable that the present sample has missed an entire class of millisecond pulsars that experience strong binary acceleration due to very massive companions in wide orbits. The discovery of such pulsars may necessitate the re-inclusion of some of the dropped terms of the geometric propagation delay.

### 3.2 Clock Corrections

Clock corrections applied by TEMPO2 may suffer from time-transfer errors present in the clock offset files provided by the user, owing either to incorrect tabulated values, or to variations in the clock offset on time scales shorter than the tabulation interval, over which linear interpolation is performed. In most instances, the dominant source of these errors will be the first step of correction, involving the local observatory clock, since observatory time standards and time transfer systems are typically less accurate than those involved in GPS and UTC time keeping. As an example of the level at which time transfer errors may occur, we note that differencing of two independent time transfer systems at the Parkes observatory leads to an error term with a root-mean-squared (rms) deviation of 8 ns over the last three years (Fig. 1). Time transfer to UTC from GPS or one of the national time standards contributing to UTC also leads to significant error, with a typical rms of  $\sim 5$  ns (Lewandowski et al. 2005).

In addition to clock correction errors, the “corrected” time of arrival, as measured against a specified realisation of TT will differ from that measured against an ideal TT, owing to instability in the contributing atomic clock systems. An indication of the level at which instability contributes can be obtained by means of the difference between the latest revision of the BIPM realisation of TT, TT(BIPM2005), with the 2001 version of the same timescale. As shown in Fig. 2, differences exist at the  $\sim 10$  ns level, even after allowing for the absorption of a fraction of the variation by other terms in the timing model.

### 3.3 Solar system Einstein delay

The time dilation integral of Irwin & Fukushima (1999) (equation 9) includes only terms of order  $1/c^2$ , plus a mean rate correction for higher-order terms. Inaccuracies in the Solar system ephemeris lead to an estimated uncertainty of 100 ps in the

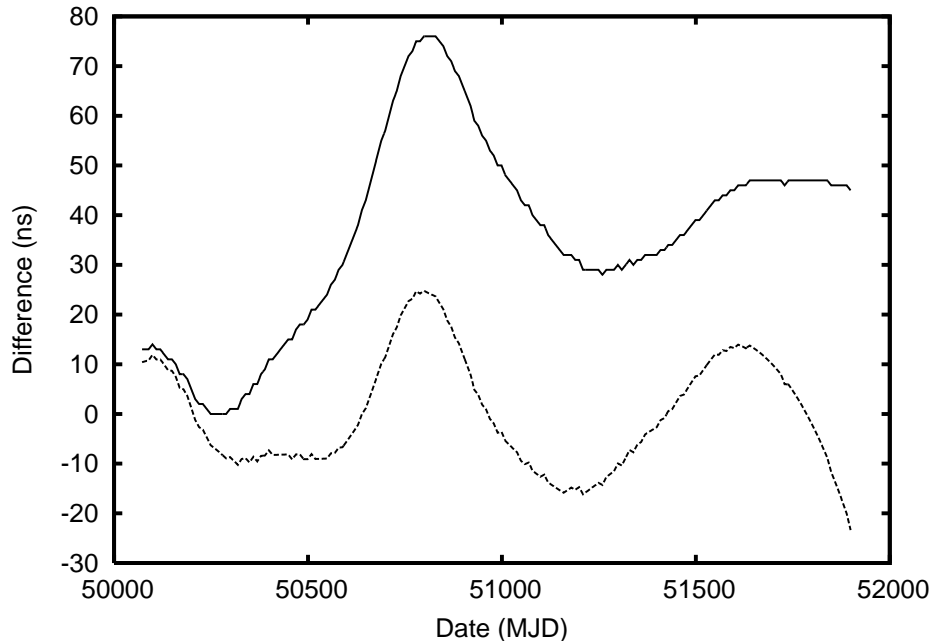


**Figure 2.** Difference between two realisations of TT, TT(BIPM2005) and TT(BIPM2001) before (solid line) and after (dashed line) removing a fitted function including a quadratic and an annual sinusoid, to account for the presence of fitted functions of this form in the timing model. The plot spans the final five years covered by TT(BIPM2001).

time integral, and  $10^{-16}$  in its derivative. The remaining higher-order terms have a maximum amplitude of 33 ps (Fukushima 1995). The effect upon the spatial coordinates of the 4-dimensional transformation relating the GCRS and BCRS is neglected. The neglected length contraction is of the order  $10^{-8} s/c$ , corresponding to up to 200 ps of excess propagation time.

### 3.4 Atmospheric delays

Equation (11) predicts the hydrostatic zenith delay to an accuracy of 0.5 mm under conditions of hydrostatic equilibrium, with variations of up to 20 mm possible under extreme weather conditions (Davis et al. 1985). These correspond to timing errors of  $1.7 - 67 \text{ ps} \cdot \text{csc } \Theta$ . In addition, the accuracy Niell mapping function degrades at small elevation angles (Niell 1996), leading to  $\sim 30 \text{ ps}$  of error at  $\Theta = 5^\circ$ . Should the user not provide tabulated surface atmospheric pressure, the use of a constant value leads to errors of the order of  $1 \text{ ns} \cdot \text{csc } \Theta$ . Likewise, lack of tabulated values for the zenith wet delay results in error at the level of  $\sim 1 \text{ ns} \cdot \text{csc } \Theta$ .

As noted in Section 2.5.2, the dispersive component of the ionosphere causes propagation delays of the order of  $7-130 \text{ ns} \cdot (f/1 \text{ GHz})^{-2}$ , where  $f$  is the observing frequency. Such effects must be removed by fitting for a time-variable dispersion measure with the aid of multi-frequency observations.

### 3.5 Solar system Roemer delay

The Roemer delay depends on the position of the observatory in the terrestrial frame, provided as input to TEMPO2. An accuracy of 30 cm is needed to meet the 1 ns criterion. In many cases the position is known to an accuracy of a few centimetres, by means of VLBI or other geodesy techniques. In addition, most sites are subject to continental drift at a rate of a few centimetres per year, which is neglected by TEMPO2. This may be remedied in future when the sensitivity and time span of observational data dictates it.

The transformation of the observatory position from the terrestrial to celestial reference frame depends on a knowledge of the Earth orientation parameters. Our requirement of 1 ns precision corresponds to maximum 10 mas of angular displacement on the surface of the Earth, or  $600 \mu\text{s}$  in UT1, the time scale tied to Earth rotation<sup>7</sup>. TEMPO2 uses the “C04” Earth orientation parameter series of the IERS, which exceeds the required precision for all dates after 1980. The effects of diurnal and subdiurnal

<sup>7</sup> Errors in UT1 relate in fact to a position offset, and should not be confused with errors that appear directly in the timing model (such as clock corrections). This is why the precision demanded of UT1 is some 600,000 times higher than the required timing accuracy.

tides are removed from the series, resulting in an additional error of at most 0.7 mas in the location of the pole, and  ${}^{+50}_{-80} \mu\text{s}$  in UT1. The IAU2000B precession-nutation model used by TEMPO2 is accurate to 1 mas.

As noted in Section 2.5.3, TEMPO2 applies transformations to the input and output values of the Solar system ephemeris that are specific to recent JPL ephemerides. Should a different ephemeris be specified, it is important that the offset of the input time parameter, and the scale of input time and output spatial vectors match those of DE405, as specified by Irwin & Fukushima (1999). Likewise, it is important that the ephemeris coordinate frame is rotationally aligned with the ICRS, for while the gross effect of a frame rotation on  $\mathbf{r}_{\oplus} \cdot \hat{\mathbf{R}}_0$  could be absorbed in the fitted pulsar position, the resultant changes in  $\hat{\mathbf{R}}_0$  will induce an error in  $\mathbf{s} \cdot \hat{\mathbf{R}}_0$  with a diurnal signature. For example, the coordinate frame of the earlier DE200 ephemeris is offset from the ICRS by  $\sim 14$  mas (Folkner et al. 1994), resulting in up to  $\pm 1.4$  ns of error.

Ultimately the accuracy of the Roemer delay hinges upon the chosen Solar system ephemeris. Preliminary investigations indicate that errors in the Solar system ephemeris may be significant and indeed measurable in pulsar timing data.

### 3.6 Solar system Shapiro delays

TEMPO2 includes the first-order Shapiro delay due all bodies for which the excess delay exceeds 0.5 ns (see Paper I). The next largest effect is due to Mars, with 60 ps of delay. The second order term is included only for the Sun. The next largest effect is due to Jupiter, with a maximum amplitude of 5 ps. Further terms appear for the Sun at the 500 ps level (Richter & Matzner 1983).

### 3.7 Interstellar propagation delays

The treatment of TEMPO2 is precise in the limit of cold plasma dispersion with negligible refraction. In practise, turbulence in the interstellar medium leads to stochastic refraction and scattering of incident radio waves, giving rise not only to familiar scintillation effects, but also to frequency-dependent variable propagation delays (Foster & Cordes 1990). Such delays arise both due to differences in the propagation path length, and also due to induced errors in the computed Roemer delay, owing to the variations in apparent source direction. According to simulations conducted by Foster & Cordes (1990), the amplitude of these terms in the selected pulsars is of the order of hundreds of nanoseconds, for observations conducted at  $\lambda \sim 20$  cm. For future, more sensitive telescopes, these errors will almost certainly dominate over radiometer noise unless steps are taken to correct for the effect or avoid it by observing at higher frequencies.

### 3.8 Transformation from SSB to BB frame

The transformation from the relativistic coordinate frames of the SSB and BB is modelled as a rotationless Lorentz transformation. This is a pure special relativistic transformation that assumes that the space-time metric tensors are completely determined by bodies in the Solar system and binary system respectively. Under general relativity this assumption will be violated by the presence of gravitational waves from external sources, causing unmodelled effects in the pulse times of arrival. Indeed, the detection of the gravitational wave background is one of the main aims of contemporary pulsar timing campaigns. Jenet et al. (2005) conducted simulations of a number of different hypothetical datasets to test the detectability of a gravitational wave background at the level predicted by theory. A significant detection was predicted for several simulated datasets of a standard optimistically within reach of current observing programs, for which the minimum detectable systematic effect (as indicated by the rms measurement error divided by the square root of the number of independent observations) is one to several nanoseconds.

### 3.9 Binary orbital effects

The principal source of error in the formulation of the timing delay due to the presence of a binary companion is the use of equations of motion derived at only the first post-Newtonian order (Damour & Deruelle 1986). To date no complete timing formula accurate at the second post-Newtonian (2PN) order has been constructed, although the orbital motion has been derived by Wex (1995), including a proper-time representation that thereby provides the 2PN Einstein delay. The largest discrepancies are due to the 2PN contribution to the rate of periastron advance, and the effect of spin-orbit interaction on the periastron advance and orbital orientation (Damour & Taylor 1992), though these effects can be absorbed in changes to  $\dot{\omega}$  and  $\dot{x}$ . The 2PN corrections to the quasi-periodic Einstein delay are of the order 80 ns for PSR B1913+16 (Wex 1995). Additional unmodelled effects include the modification to the Shapiro delay due to the gravitomagnetic field of a spinning companion (Laguna & Wolszczan 1997), and the effect of gravitational light bending on the apparent rotational phase of the pulsar beam (Schneider 1990; Doroshenko & Kopeikin 1995), which cannot be separately measured (Wex & Kopeikin 1999). For double-neutron-star binaries, all of these effects are quite large compared to our 1 ns accuracy goal, especially for nearly

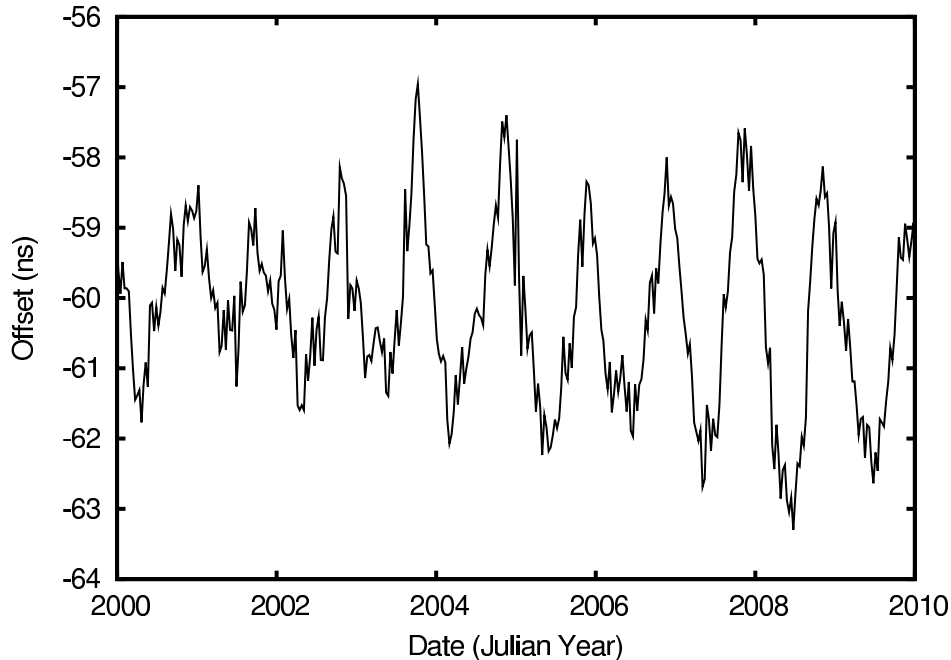


**Figure 3.** Difference between timing models of TEMPO2 and TEMPO owing to the use of different numerical approximations to the Solar system time dilation integral.

edge-on orbits, however it so happens that the binary evolutionary history of such systems rarely results in a pulsar that is spinning rapidly enough to provide timing measurements of high accuracy.

Only since the discovery of PSR J0737–3039A, a 22-ms pulsar in a highly inclined compact orbit with a second pulsar (Lyne et al. 2004), has the measurability of these effects been seriously considered. It is expected that the 2PN contribution to  $\dot{\omega}$  will be measurable in coming years (Kramer et al. 2006b). Although this effect is easily accommodated in the existing binary model, we understand that efforts are underway to develop a fully consistent 2PN timing formula. Incorporation of this formula in TEMPO2 would be highly desirable for assurance that the model will continue to be accurate at the level demanded by ever-decreasing measurement errors and potentially more extreme binaries discovered in coming decades.

It should be noted that owing to approximations made in the orbital kinematics, the Laplace-Lagrange parameterisation is only valid for orbits of low eccentricity. The error term is of order  $xe^2$  (Lange et al. 2001).

## 4 DIFFERENCES FROM TEMPO

### 4.1 Tropospheric delays

TEMPO makes no attempt to model non-dispersive atmospheric delays. These are dominated by the hydrostatic delay (Section 2.5.2), which is a mainly diurnal term of up to tens of nanoseconds in amplitude, depending on the elevation angle distribution.

### 4.2 Einstein delay

To compute a version of the time dilation integral of equation (9), TEMPO uses the series approximation of Fairhead & Bretagnon (1990), since shown to be significantly in error (Fukushima 1995; Irwin & Fukushima 1999). An example of the discrepancy is shown in Fig. 3, which plots the difference in barycentric time as computed by TEMPO2 and TEMPO. The comparison is made in terms of the now-obsolete Barycentric Dynamical Time (TDB, see below), as used by TEMPO. The difference consists mainly of a constant offset of  $\sim 60$  ns, an annual term of  $\sim 2$  ns amplitude, and a small noise-like contribution due to truncation of the internal Chebyshev representation used by TEMPO. The constant offset is immaterial since the zero point of TDB has never been well-defined. It arises for the most part due to the use by Irwin & Fukushima (1999) of an erroneous estimate of the offset between TDB and  $T_{\text{eph}}$ , with an additional  $\sim 6$  ns due to software errors in early versions of the Fairhead & Bretagnon (1990) Fortran code, which only manifest on certain computer systems (P. Wallace, personal communication). The annual term, probably due to inaccuracies in the Fairhead & Bretagnon (1990) series, will act to corrupt the source position at the 0.5 microarcsec level, as fitted by TEMPO.

It should also be noted that the time integral actually computed by Fairhead & Bretagnon (1990) and Irwin & Fukushima

(1999) includes a negative term in the integrand designed to give a long-term zero mean value of the integral. Unlike TEMPO2, TEMPO does not add a counteracting linear term to the result, causing an overall difference in the scale of the barycentric coordinate timescale. In the case of TEMPO the resultant time refers to the  $T_{\text{eph}}$  timescale (Section 2.5.1), which is approximately equivalent to the ill-defined IAU predecessor to TCB, known as TDB (see Standish 1998). The continued use of  $T_{\text{eph}}$  or TDB as a barycentric coordinate time for pulsar timing is deprecated, since under this condition the scale of units of fitted parameters involving length and/or time differ subtly from the standard SI definition and fail to comply with IAU Resolutions: see Paper I.

### 4.3 Earth orientation

In its calculation of the observatory position in the barycentric frame, TEMPO uses the IAU 1976 precession (Lieske et al. 1977) and IAU 1980 nutation (Seidelmann 1982) theories, which are in error at the 50 mas level. More significantly, it also neglects polar motion, which amounts to up to  $\pm 300$  mas, corresponding to up to  $\pm 35$  ns of timing error, with a variable diurnal signature. The polar motion error is dominated by two periodicities, one with a period of one year (due to seasonal influences on oceans and the atmosphere), and the other with a period of 435 days (the Chandler wobble, due to free precession)—see Paper I. Depending on the site position, source direction and hour angle distribution, part of the annual polar motion may enter the timing model as an annual term at the level of up to  $\sim 10$  ns, corrupting the fitted pulsar position at the level of a few microarcsec.

### 4.4 Shapiro delays

TEMPO includes only the first-order Shapiro delay term due to the Sun. Terms of up to 180 ns for the planetary Shapiro delays, and 9 ns for the second-order term of the Solar Shapiro delay were omitted.

### 4.5 Dispersion

TEMPO includes some small errors in the transformation of the observing frequency to the barycentric reference frame. Firstly, the computation of the site velocity (equation 27) neglected polar motion, precession and nutation. Polar motion changes the direction of the velocity vector  $\hat{x}$  by up to 300 mas, altering its projection on the line of sight by up to  $\sim 10^{-10}c$  and corrupting the dispersion term  $\Delta_{\text{IS}}$  of equation (37) by a fractional amount  $\sim 10^{-9.5}$ . More significantly, precession moves the vector by  $\sim 20$  arcsec  $\text{yr}^{-1}$ , leading to a fractional error in  $\Delta_{\text{IS}}$  with an amplitude increasing at a rate of up to  $\sim 2 \times 10^{-8} \text{yr}^{-1}$ . This will manifest as an apparent annual variation in the dispersion measure, with an amplitude equal to  $\sim \text{DM} \cdot 10^{-8}t/\text{yr}$ , where  $t$  is the time elapsed since Julian year 2000.0. For single-frequency datasets, the effect would be absorbed by the annual proper motion term, corrupting it at the  $\sim 10 \mu\text{as yr}^{-1}$  level.

Secondly, TEMPO neglected to account for the Einstein rate (Section 2.6.1). The use by TEMPO of TDB instead of TCG (Section 4.2) removes a large positive mean from the Einstein rate, leaving residual rate errors at the  $10^{-9.5}$  level, mostly modulated with an annual periodicity. This corresponds to fractional errors in  $\Delta_{\text{IS}}$  at the  $10^{-9}$  level.

### 4.6 Secular and binary motion

The full geometric time delay of equation (5) contains several terms involving the displacement of the pulsar due to secular motion ( $\mathbf{k}$ ). Of these, TEMPO includes only those terms related both to secular and annual motion. In doing so, it neglected direct Doppler shift (which includes both classical and relativistic terms) due to radial velocity and its change in time due to radial acceleration, and the Shklovskii effect and its change over time due to the radial motion and transverse acceleration. None of these omissions is necessarily problematic, because all can be absorbed in a redefinition of other measured parameters. In TEMPO2 they are provided directly so that advantage may be taken of additional constraints that may be available: for example, if the intrinsic spin orbital period derivative is known to be small, it can be held fixed at zero and the distance determined directly via the Shklovskii effect.

The public distribution of TEMPO also omits the Kopeikin terms, however the secular changes to the viewing geometry may be absorbed in other parameters, while modified versions of TEMPO exist that include the annual-orbital parallax. The orbital parallax, not modelled in any known version of TEMPO, contributes a timing term of up to 30 ns in amplitude.

## 5 SUMMARY AND CONCLUSIONS

We have presented a model for pulsar pulse times of arrival that exceeds all previous efforts in its accuracy. This timing model is the basis of TEMPO2, a new software package for pulsar timing. The goal of TEMPO2 to provide accuracy at the

1-nanosecond level is largely satisfied by the model presented here, the exception being pulsars that are part of extremely relativistic binary systems. Further theoretical work on second- and higher-order relativistic effects will be required before progress can be made in this area. Fortunately, the pulsars for which the most precise measurements are possible tend not to be part of such relativistic binaries.

Terrestrial clock instability, Solar system ephemeris errors and the local gravitational wave background stand as the likely sources of significant systematic error. Pulsar timing array campaigns should eventually be able to provide measurements of these effects, allowing for their removal from the residuals and more importantly providing a valuable insight into the causative physical processes.

With the next generation of radio telescopes, such as the Square Kilometre Array, achievable measurement error will be reduced in some cases to below 10 ns. For systematic effects, the timing model presented here should remain applicable in most cases, and will present a useful starting point for extension if necessary. However, at this level of precision previously negligible stochastic effects will come into play. Possibly the most problematic of these will be the effect of interstellar scattering.

## **ACKNOWLEDGEMENTS**

The authors wish to thank M. Kramer for comments that improved the manuscript, and A. Irwin, J. Weisberg, P. Wallace and M. Kramer for useful discussions.

**APPENDIX A: TABLES OF PARAMETERS AND VARIABLES**



**Table A1.** Parameters of the timing model

Algebraic	Name		Description	Section
		ASCII		
$\alpha$		RA	Right ascension of pulsar (ICRS)	2.5.3
$\beta$		ELAT	Ecliptic latitude of pulsar	2.5.3
$\gamma$		GAMMA	Amplitude of binary Einstein delay	2.7.4
$\Delta\phi_n$		GLPH_ $n$	Pulse phase increment for glitch $n$	2.8
$\Delta\nu_n$		GLF0_ $n$	Pulse frequency increment for glitch $n$	2.8
$\Delta\dot{\nu}_n$		GLF1_ $n$	Pulse frequency derivative increment for glitch $n$	2.8
$\Delta\nu_{tn}$		GLF0D_ $n$	Amplitude of decaying pulse frequency term for glitch $n$	2.8
$\delta$		DEC	Declination of pulsar (ICRS)	2.5.3
$\delta_\theta$		DTHETA	Relativistic longitudinal deformation of orbit	2.7.2
$\delta_r$		DR	Relativistic radial deformation of orbit	2.7.2
$\epsilon_0$		ECLOBL	Mean obliquity of the ecliptic at J2000.0	2.5.3
$\zeta$		FDDI	Exponent of frequency-dependent delay	2.6
$\eta_0$		EPS1	First Laplace-Lagrange parameter at $t^{\text{psr}} = T_0$	2.7.6
$\dot{\eta}$		EPS1DOT	Time derivative of first Laplace-Lagrange parameter	2.7.6
$\kappa_0$		EPS2	Second Laplace-Lagrange parameter at $t^{\text{psr}} = T_0$	2.7.6
$\dot{\kappa}$		EPS2DOT	Time derivative of second Laplace-Lagrange parameter	2.7.6
$\lambda$		ELONG	Ecliptic longitude of pulsar	2.5.3
$\mu_\alpha$		PMRA	Proper motion in right ascension	2.5.3
$\mu_{\alpha B}$		KPMRA	Proper motion in right ascension for Kopeikin term	2.7.2
$\mu_\beta$		PMELAT	Proper motion in ecliptic latitude	2.5.3
$\mu_{\beta B}$		KPMELAT	Proper motion in ecliptic latitude for Kopeikin term	2.7.2
$\mu_\delta$		PMDEC	Proper motion in declination	2.5.3
$\mu_{\delta B}$		KPMDEC	Proper motion in declination for Kopeikin term	2.7.2
$\mu_\lambda$		PMELONG	Proper motion in ecliptic longitude	2.5.3
$\mu_{\lambda B}$		KPMELONG	Proper motion in ecliptic longitude for Kopeikin term	2.7.2
$\mu_\parallel$		PMRV	Radial proper motion	2.5.3
$\nu^{(n)}$		F $n$	$n$ -th time derivative of pulse frequency at $t^{\text{psr}} = t_{\text{freq}}$	2.8
csc $\xi$		SPINCSCI	Cosecant of inclination angle of spin axis	2.7.5
$\Pi$		PX	Annual parallax	2.5.3
$\tau_{gn}$		GLTD_ $n$	Time constant for glitch $n$	2.8
$\phi_0$			Pulse phase at $t^{\text{psr}} = t_{\text{freq}}$ (implicit floating parameter)	2.8
$\chi$		SPINPA	Position angle of spin axis w.r.t $\Omega$	2.7.5
$\Omega$		KOM	Position angle of ascending node	2.7.1, 2.7.2
$\omega_0$		OM	Longitude of periastron at $t^{\text{psr}} = T_0$	2.7.2
$\dot{\omega}$		OMDOT	Time derivative of longitude of periastron	2.7.2
$\dot{\omega}_x$		XOMDOT	Non-GR contribution to derivative of longitude of periastron	2.7.5
$\ddot{\omega}$		OM2DOT	Second time derivative of longitude of periastron	2.7.7

**Table A1** – *continued*

Algebraic	Name		Description	Section
		ASCII		
$A$		A0	First binary aberration parameter	2.7.3
$B$		B0	Second binary aberration parameter	2.7.3
$a_{\perp}$		RACC	Radial acceleration of BB-SSB	2.6.2
$a_{\mu}$		PMACC	Acceleration of BB-SSB in direction parallel to proper motion	2.6.2
$d_{\text{Shk}}$		D_SHK	Distance used for Shklovskii term	2.6.2
$d_{\text{AOP}}$		D_AOP	Distance used for annual-orbital parallax term	2.7.1
$d_{\text{OP}}$		D_OP	Distance used for orbital parallax term	2.7.1
$\text{DM}^{(n)}$		DM $n$	$n$ -th time derivative of interstellar dispersion measure	2.6.1
$e_0$		ECC	Eccentricity of binary orbit at $t^{\text{PSR}} = T_0$	2.7.2
$\dot{e}$		ECCDOT	Time derivative of eccentricity of binary orbit	2.7.2
$i$		KI	Binary orbital inclination angle used for Kopeikin terms	2.7.1,2.7.2
$k_f$		FDDC	Scale of frequency-dependent delay	2.6
$M$		MTOT	Total binary system mass	2.7.5
$m_2$		M2	Binary companion mass	2.7.5
$n_0$		NE1AU	Mean electron density at 1 AU heliocentric radius	2.5.4
$P_{\text{b0}}$		PB	Binary orbital period at $t^{\text{PSR}} = T_0$	2.7.2
$\dot{P}_{\text{b0}}$		PBDOT	Time derivative of binary orbital period	2.7.2
$\dot{P}_{\text{bx}}$		XPBDOT	Non-GR contribution to time derivative of binary orbital period	2.7.5
$r$		R	Shapiro delay range parameter	2.7.4
$s$		S	Shapiro delay shape parameter	2.7.4
$\sin i$		SINI	Sine of orbital inclination	2.7.5
$t_{\text{D}}$		DMEPOCH	Epoch of dispersion measure	2.6
$t_{\text{gn}}$		GLEP_ $n$	Epoch of $n$ -th glitch	2.8
$t_{\text{pos}}$		POSEPOCH	Epoch of position	2.2,2.3,2.5.3
$t_{\text{freq}}$		PEPOCH	Epoch of pulse frequency	2.8
$T_0$		T0	Time of periastron	2.7.2
$T_{\text{asc}}$		TASC	Time of ascending node, Laplace-Lagrange parameterisation	2.7.6
$v_{\parallel}$		RV	Radial velocity for Doppler correction	2.6.2,2.6.3
$v_{\parallel\text{Shkdot}}$		RVS	Radial velocity for secular acceleration of Shklovskii term	2.6.2
$v_{\perp}$		TV	Transverse velocity for Doppler correction	2.6.3
$x$		A1	Projected semi-major axis of binary orbit	2.7.2
$\dot{x}$		A1DOT	Time derivative of projected semi-major axis of binary orbit	2.7.2
$\ddot{x}$		X2DOT	Second time derivative of projected semi-major axis of binary orbit	2.7.7
$z_s$		SHAPMAX	Shapiro delay parameter, $z_s \equiv -\ln(1-s)$	2.7.4

**Table A2.** Other symbols used

Symbol	Description	Section
$\hat{\alpha}$	Unit vector in direction of increasing right ascension	2.5.3
$\hat{\beta}$	Unit vector in direction of increasing ecliptic latitude	2.5.3
$\Gamma$	Doppler shift due to BB–SSB velocity	2.6.3
$\Delta_{\odot}$	Solar system part of timing formula	2.5
$\Delta_A$	Atmospheric propagation delay	2.5.2
$\Delta_{AB}$	Binary aberration delay	2.7.3
$\Delta_B$	Binary part of timing formula	2.7
$\Delta_{D\odot}$	Solar system dispersion delay	2.5.4
$\Delta_{E\odot}$	Solar system Einstein delay	2.5.1
$\Delta_{E\odot-\oplus}$	Solar system Einstein delay for geocentre	2.5.1
$\Delta_{EB}$	Binary Einstein delay	2.7.4
$\Delta_{ES}$	Einstein delay due to secular motion	2.6.3
$\Delta_{FDD}$	Frequency-dependent delay	2.6.1
$\Delta_{hz}$	Atmospheric hydrostatic delay for zenith	2.5.2
$\Delta_P$	Annual parallax delay term	2.5.3
$\Delta_{ISD}$	Interstellar dispersion delay	2.6.1
$\Delta_{IS}$	Interstellar part of timing formula	2.6
$\Delta_{KB}$	Kopeikin delay	2.7.1
$\Delta_{R\odot}$	Solar system Roemer delay	2.5.3
$\Delta_{RB}$	Binary Roemer delay	2.7.1
$\Delta_{RB\parallel}$	Radial part of binary Roemer delay	2.7.1
$\Delta_{RE}$	Combined binary Roemer and Einstein delay	2.7.8
$\Delta_{S\odot}$	Solar system Shapiro delay	2.5.5
$\Delta_{S\odot 2}$	Second-order Solar Shapiro delay	2.5.5
$\Delta_{SB}$	Binary Shapiro delay	2.7.4
$\Delta_{VP}$	Interstellar vacuum propagation delay	2.6.2
$\Delta_{wz}$	Atmospheric wet delay for zenith	2.5.2
$\Delta L_C^{(PN)}$	Higher-order post-Newtonian correction to Einstein delay	2.5.1
$\Delta L_C^{(A)}$	Asteroid correction to Einstein delay	2.5.1
$\hat{\delta}$	Unit vector in direction of increasing declination	2.5.3
$\eta$	First Laplace-Lagrange parameter	2.7.6
$\Theta$	Source elevation angle	2.5.2
$\theta$	Orbital longitude	2.7.2
$\kappa$	Second Laplace-Lagrange parameter	2.7.6
$\hat{\lambda}$	Unit vector in direction of increasing ecliptic longitude	2.5.3
$\boldsymbol{\mu}$	Three-dimensional proper motion vector	2.5.3
$\rho$	Pulsar-Sun-observatory angle	2.5.4
$\phi$	Pulse phase	2.8
$\phi_{gn}$	Contribution to pulse phase by glitch $n$	2.8
$\varphi$	Geodetic latitude of the observatory	2.5.2
$\Phi$	Orbital phase-type variable for Laplace-Lagrange binary parameterisation	2.5.2
$\Phi^0$	Zeroth-order approximation to $\Phi$	2.7.8
$\psi_i$	Pulsar-telescope-object angle for $i$ -th solar system body	2.5.5
$\omega$	Longitude of periastron	2.7.2
$\boldsymbol{\omega}_{\oplus}$	Angular velocity of Earth rotation	2.5.3

**Table A2** – *continued*

Symbol	Description	Section
$A_e(u)$	True anomaly of orbit as a function of eccentric anomaly	2.7.2
$\mathbf{a}$	Acceleration vector of BB - SSB	2.3, 2.6.2
$a$	Semi-major axis of pulsar orbit	2.7.2
$\mathbf{b}$	Vector from BB to pulsar	2.3, 2.7.2
$c$	Vacuum speed of light $\equiv 2.99792458 \times 10^8$ m s <sup>-1</sup>	
$C$	Convenience variable in binary motion	2.7.2
$d_p$	Parallax distance $\equiv 1$ AU/ $\Pi$	2.5.3
$e, e_\theta, e_r$	Orbital eccentricities	2.7.2
$\mathbf{e}_1, \mathbf{e}_2$	Basis vectors in plane of sky (i.e. $\hat{\alpha}, \hat{\delta}$ or $\hat{\lambda}, \hat{\beta}$ )	2.7.2
$D$	Interstellar dispersion constant	2.6.1
DM	Interstellar dispersion measure	2.6.1
$\mathbf{E}$	Matrix relating equatorial and ecliptic coordinates	2.5.3
$f$	Frequency of electromagnetic wave	2.5.4, 2.6.1
$f^{\text{SSB}}$	Frequency of electromagnetic wave in SSB frame	2.5.4, 2.6.1
$G$	Gravitational constant	
$H$	Height of observatory above the geoid	2.5.2
$i$	Orbital inclination angle	2.7.2
$\mathbf{k}$	Displacement of BB since $t^{\text{SSB}} = t_{\text{pos}}$	2.3, 2.5.3, 2.6.2
$k$	Derivative of longitude of periastron w.r.t. true anomaly	2.7.2
$k_D$	Constant of proportionality relating $D$ and DM	2.6.1
$m_2$	Binary companion mass	2.7.4
$m_h(\Theta)$	Mapping function for hydrostatic propagation delay	2.5.2
$m_w(\Theta)$	Mapping function for wet propagation delay	2.5.2
$n$	Mean angular frequency of binary since $T_0$	2.7.2
$P$	Surface atmospheric pressure	2.5.2
$P_b$	Binary orbital period	2.7.2
$\mathbf{Q}$	Frame bias, precession and nutation matrix	2.5.3
$\mathbf{R}$	Earth rotation matrix	2.5.3
$\mathbf{r}$	BCRS position vector of observatory	2.3, 2.5.3
$\mathbf{r}_\oplus$	BCRS position vector of geocentre	2.5.1, 2.5.3
$\mathbf{R}$	BCRS displacement vector of pulsar minus observatory	2.3
$\mathbf{R}_0$	BCRS position vector of binary barycentre at $t^{\text{SSB}} = t_{\text{pos}}$	2.3
$\mathbf{R}_{\text{BB}}$	BCRS position vector of BB at time of observation	2.5.3
$\hat{\mathbf{R}}_{\text{BB}}$	BCRS direction unit vector of BB at time of observation	2.5.3
$\mathbf{s}$	GCRS position vector of observatory	2.5.1, 2.5.3
$S$	Convenience variable in binary motion	2.7.2
$s_{\text{IS}}$	ISM part of geometric path length (minus value at $t^{\text{SSB}} = t_{\text{pos}}$ )	2.6.2
$s_{\text{B}}$	Binary orbital part of geometric path length	2.7.1
$t_0$	Common epoch of TT, TCG and TCB	2.5.1
$t^{\text{obs}}$	Terrestrial Time ( $\sim$ proper time) at observatory	2.2
$t^{\text{SSB}}$	Barycentric Coordinate Time	2.2
$t^{\text{BB}}$	Coordinate time in frame of binary barycentre	2.2
$t^{\text{psr}}$	Proper time in pulsar frame	2.2
$t_e^{\text{psr}}$	Proper time of emission of pulse	2.2
$t_a^{\text{frame}}$	Time of arrival of pulse in a given frame	2.2
$T_\odot$	$GM_\odot/c^3$ , half the light travel time across the Solar Schwarzschild radius	2.7.4
$U_\oplus$	Gravitational potential at the geocentre due to SS bodies	2.5.1
$u$	Eccentric anomaly of orbit	2.7.2
$v_\oplus$	Velocity of the geocentre relative to the SSB	2.5.1
$\mathbf{W}$	Polar motion matrix	2.5.3
$W_0$	Gravitational plus spin potential of Earth at the geoid	2.5.1

## REFERENCES

- Anderson J., ed. 1999, Proc. of the Twenty-Third General Assembly, Trans. IAU, XXIII B
- Arzoumanian Z., Joshi K., Rasio F., Thorsett S. E., 1996, in Johnston S., Walker M. A., Bailes M., eds, Pulsars: Problems and Progress, IAU Colloquium 160 Orbital parameters of the PSR B1620–26 triple system. Astronomical Society of the Pacific, San Francisco, pp 525–530
- Backer D. C., Hellings R. W., 1986, *Ann. Rev. Astr. Ap.*, 24, 537
- Bell J. F., Bailes M., 1996, *ApJ*, 456, L33
- Bilitza D., 2001, *Radio Sci.*, 36, 261
- Blandford R., Teukolsky S. A., 1976, *ApJ*, 205, 580
- Camilo F., Thorsett S. E., Kulkarni S. R., 1994, *ApJ*, 421, L15
- Cognard I., Bourgois G., Lestrade J.-F., Biraud F., Aubry D., Darchy B., Drouhin J.-P., 1996, *A&A*, 311, 179
- Damour T., Deruelle N., 1986, *Ann. Inst. H. Poincaré (Physique Théorique)*, 44, 263
- Damour T., Taylor J. H., 1991, *ApJ*, 366, 501
- Damour T., Taylor J. H., 1992, *Phys. Rev. D*, 45, 1840
- Davis J. L., Herring T. A., Shapiro I. I., Rogers A. E. E., Elgered G., 1985, *Radio Sci.*, 20, 1593
- Doroshenko O. V., Kopeikin S. M., 1995, *MNRAS*, 274, 1029
- Fairhead L., Bretagnon P., 1990, *A&A*, 229, 240
- Folkner W. M., Charlot P., Finger M. H., Williams J. G., Sovers O. J., Newhall X., Standish E. M., 1994, *A&A*, 287, 279
- Foster R. S., Cordes J. M., 1990, *ApJ*, 364, 123
- Freire P. C., Camilo F., Lorimer D. R., Lyne A. G., Manchester R. N., D’Amico N., 2001, *MNRAS*, 326, 901
- Fukushima T., 1995, *A&A*, 294, 895
- Harada W., Fukushima T., 2004, *AJ*, 127, 531
- Hellings R. W., 1986, *AJ*, 91, 650
- Hobbs G. M., Edwards R. T., Manchester R. N., 2006, *MNRAS*, 369, 655
- Irwin A. W., Fukushima T., 1999, *A&A*, 348, 642
- Issautier K., Hoang S., Moncuquet M., Meyer-Vernet N., 2001, *Space Sci. Rev.*, 97, 105
- Issautier K., Meyer-Vernet N., Moncuquet M., Hoang S., 1998, *J. Geophys. Res.*, 103, 1969
- Jenet F. A., Hobbs G. B., Lee K. J., Manchester R. N., 2005, *ApJ*, 625, L123
- Jenet F. A., Hobbs G. H., Lee K. J., Manchester R. N., 2005, *ApJ*, 625, L123
- Kaspi V. M., Taylor J. H., Ryba M., 1994, *ApJ*, 428, 713
- Kopeikin S. M., 1995, *ApJ*, 439, L5
- Kopeikin S. M., 1996, *ApJ*, 467, L93
- Kramer M., Stairs I. H., Manchester R. N., McLaughlin M. A., Lyne A. G., Ferdman R. D., Burgay M., Lorimer D. R., Possenti A., D’Amico N., Sarkissian J. M., Reynolds J. E., Joshi B. C., Freire P. C. C., Camilo F., 2006b, *Nature*
- Kramer M., Stairs I. H., Manchester R. N., McLaughlin M. A., Lyne A. G., Ferdman R. D., Burgay M., Lorimer D. R., Possenti A., D’Amico N., Sarkissian J. M., Reynolds J. E., Joshi B. C., Freire P. C. C., Camilo F., 2006a, *Annalen der Physik*, 15, 34
- Laguna P., Wolszczan A., 1997, *ApJ*, 486, L27
- Lai D., Bildsten L., Kaspi V. M., 1995, *ApJ*, 452, 819
- Lange C., Camilo F., Wex N., Kramer M., Backer D., Lyne A., Doroshenko O., 2001, *MNRAS*, 326, 274
- Lewandowski W., Matsakis D., Panfilo G., P. T., 2005, in Proc. 36th PTTI First evaluation and experimental results on the determination of uncertainties in [UTC - UTC(k)]. pp 247–261
- Lieske J. H., Lederle T., Fricke W., Morando B., 1977, *A&A*, 58, 1
- Lorimer, D. R. and Kramer, M. 2005, *Handbook of Pulsar Astronomy*. Cambridge University Press
- Lyne A. G., Burgay M., Kramer M., Possenti A., Manchester R. N., Camilo F., McLaughlin M. A., Lorimer D. R., D’Amico N., Joshi B. C., Reynolds J., Freire P. C. C., 2004, *Science*, 303, 1153
- McCarthy D. D., Luzum B. J., 2003, *Celest. Mech. and Dynamical Astron.*, 85, 37
- McCarthy D. D., Petit G., eds, 2004, *IERS Conventions 2003*, IERS Technical Note 32. Verlag des Bundesamts für Kartographie und Geodäsie, Frankfurt am Main
- MacMillan D. S., 1995, *Geophys. Res. Lett.*, 22, 1041
- Mamoru S., Kondo T., Kawai E., 2003, *Radio Sci.*, 38, 1069
- Manchester R. N., Hobbs G. B., Teoh A., Hobbs M., 2005, *AJ*, 129, 1993
- Nice D. J., Splaver E. M., Stairs I. H., 2001, *ApJ*, 549, 516
- Niell A. E., 1996, *J. Geophys. Res.*, 101, 3227
- Niell A. E., Coster A. J., Solheim F. S., Mendes V. B., Toor P. C., Langley R. B., Upham C. A., 2001, *J. Atmos. and Oceanic Technol.*, 18, 830

- Phillips J. A., Wolszczan A., 1992, *ApJ*, 385, 273  
Richter G. W., Matzner R. A., 1983, *Phys. Rev. D*, 28, 3007  
Rickman H., ed. 2001, *Proc. of the Twenty-Fourth General Assembly, Trans. IAU, XXIV B*  
Sandhu J. S., Bailes M., Manchester R. N., Navarro J., Kulkarni S. R., Anderson S. B., 1997, *ApJ*, 478, L95  
Schaer S., 1999, PhD thesis, Bern Univ.  
Scherer K., Fichtner H., Anderson J. D., Lau E. L., 1997, *Science*, 278, 1919  
Schneider J., 1990, *A&A*, 232, 62  
Seidelmann P. K., 1982, *Celest. Mech.*, 27, 79  
Shklovskii I. S., 1970, *Sov. Astron.*, 13, 562  
Splaver E. M., Nice D. J., Stairs I. H., Lommen A. N., Backer D. C., 2005, *ApJ*, 620, 405  
Stairs I. H., Thorsett S. E., Arzoumanian Z., 2004, *Phys. Rev. Lett.*, 93, 141101  
Standish E. M., 1998, *JPL Planetary and Lunar Ephemerides, DE405/LE405, Memo IOM 312.F-98-048. JPL, Pasadena*  
Standish E. M., 1998, *A&A*, 336, 381  
Taylor J. H., Fowler L. A., McCulloch P. M., 1979, *Nature*, 277, 437  
Taylor J. H., Weisberg J. M., 1989, *ApJ*, 345, 434  
van Straten W., 2003, PhD thesis, Swinburne University of Technology  
van Straten W., 2004, *ApJS*, 152, 129  
van Straten W., Bailes M., Britton M., Kulkarni S. R., Anderson S. B., Manchester R. N., Sarkissian J., 2001, *Nature*, 412, 158  
Weisberg J. M., Taylor J. H., 2002, *ApJ*, 576, 942  
Wex N., 1995, *Class. Quantum Grav.*, 12, 983  
Wex N., 1998, *MNRAS*, 298, 67  
Wex N., Kopeikin S., 1999, *ApJ*, 513, 388  
Wolszczan A., Frail D. A., 1992, *Nature*, 355, 145  
Wolszczan A., Hoffman I. M., Konacki M., Anderson S. B., Xilouris K. M., 2000, *ApJ*, 540, L41